Calhoun: The NPS Institutional Archive

DSpace Repository

Theses and Dissertations | 1. Thesis and Dissertation Collection, all items

2020-03

MODELING ACOUSTIC PROPAGATION FROM CONICAL SHAPED AND STANDARD BLOCK EXPLOSIVE SOURCES IN COMPLEX OCEAN ENVIRONMENTS

Chiu, Wei-Ming

Monterey, CA; Naval Postgraduate School

http://hdl.handle.net/10945/64841

Downloaded from NPS Archive: Calhoun

Calhoun is a project of the Dudley Knox Library at NPS, furthering the precepts and goals of open government and government transparency. All information contained herein has been approved for release by the NPS Public Affairs Officer.

Dudley Knox Library / Naval Postgraduate School
411 Dyer Road / 1 University Circle
Monterey, California USA 93943

http://www.nps.edu/library

NAVAL POSTGRADUATE SCHOOL

MONTEREY, CALIFORNIA

THESIS

MODELING ACOUSTIC PROPAGATION FROM CONICAL SHAPED AND STANDARD BLOCK EXPLOSIVE SOURCES IN COMPLEX OCEAN ENVIRONMENTS

by

Wei-Ming Chiu

March 2020

Thesis Advisor: Derek Olson
Co-Advisor: Joseph P. Hooper

Approved for public release. Distribution is unlimited.

THIS PAGE INTENTIONALLY LEFT BLANK

REPORT DOCUMENTATION PAGE	*Form Approved OMB No. 0704-0188*

Public reporting burden for this collection of information is estimated to average 1 hour per response, including the time for reviewing instruction, searching existing data sources, gathering and maintaining the data needed, and completing and reviewing the collection of information. Send comments regarding this burden estimate or any other aspect of this collection of information, including suggestions for reducing this burden, to Washington headquarters Services, Directorate for Information Operations and Reports, 1215 Jefferson Davis Highway, Suite 1204, Arlington, VA 22202-4302, and to the Office of Management and Budget, Paperwork Reduction Project (0704-0188) Washington, DC 20503.

1. AGENCY USE ONLY *(Leave blank)*	**2. REPORT DATE** March 2020	**3. REPORT TYPE AND DATES COVERED** Master's thesis

4. TITLE AND SUBTITLE
MODELING ACOUSTIC PROPAGATION FROM CONICAL SHAPED AND STANDARD BLOCK EXPLOSIVE SOURCES IN COMPLEX OCEAN ENVIRONMENTS

5. FUNDING NUMBERS

6. AUTHOR(S) Wei-Ming Chiu

7. PERFORMING ORGANIZATION NAME(S) AND ADDRESS(ES)
Naval Postgraduate School
Monterey, CA 93943-5000

8. PERFORMING ORGANIZATION REPORT NUMBER

9. SPONSORING / MONITORING AGENCY NAME(S) AND ADDRESS(ES)
N/A

10. SPONSORING / MONITORING AGENCY REPORT NUMBER

11. SUPPLEMENTARY NOTES The views expressed in this thesis are those of the author and do not reflect the official policy or position of the Department of Defense or the U.S. Government.

12a. DISTRIBUTION / AVAILABILITY STATEMENT
Approved for public release. Distribution is unlimited.

12b. DISTRIBUTION CODE
A

13. ABSTRACT (maximum 200 words)

Detection of underwater explosions by acoustic means, which has been widely researched, is simple, given the large peak pressures produced by these types of sources. By contrast, estimation of the explosive yield and type of explosive by such means has received less attention. This research compares the propagation of acoustic waves in a shallow water waveguide generated by underwater detonations producing broadband impulse signals. Typically, broadband waves are dispersive due to the waveguide in shallow water regions. Data was drawn from experiments conducted near Oahu, Hawai'i, using two explosive sources for different configurations: a conical shaped charge and a standard block. Both sources consisted of Composition C-4 explosive material and were detonated at comparable depths. This thesis focuses on differentiating the propagation of acoustic waves in multiple environments from these two kinds of sources. Simulations were used to explore different seabed properties, which varied by location, and how they impacted peak pressure variability across the Indo-Pacific region. By enhancing the understanding of acoustic propagation of explosive sources in complex environments, this research is helpful in cross domain operations. The developed models can also be applied defensively to determine the optimal placement and number of sensors required to monitor critical infrastructure on the seabed.

14. SUBJECT TERMS	**15. NUMBER OF PAGES**
acoustic propagation, waveguide dispersion, broadband explosive source, underwater ocean environment, sedimentation, geo-acoustic properties, conical shaped charge explosive, standard block C-4, normal mode theory, data analysis	87
	16. PRICE CODE

17. SECURITY CLASSIFICATION OF REPORT	**18. SECURITY CLASSIFICATION OF THIS PAGE**	**19. SECURITY CLASSIFICATION OF ABSTRACT**	**20. LIMITATION OF ABSTRACT**
Unclassified	Unclassified	Unclassified	UU

NSN 7540-01-280-5500

Standard Form 298 (Rev. 2-89)
Prescribed by ANSI Std. 239-18

THIS PAGE INTENTIONALLY LEFT BLANK

Approved for public release. Distribution is unlimited.

MODELING ACOUSTIC PROPAGATION FROM CONICAL SHAPED AND STANDARD BLOCK EXPLOSIVE SOURCES IN COMPLEX OCEAN ENVIRONMENTS

Wei-Ming Chiu
Lieutenant, Taiwan Navy
BSCE, The Citadel, 2013

Submitted in partial fulfillment of the
requirements for the degrees of

MASTER OF SCIENCE IN PHYSICAL OCEANOGRAPHY

and

MASTER OF SCIENCE IN ENGINEERING ACOUSTICS

from the

NAVAL POSTGRADUATE SCHOOL
March 2020

Approved by: Derek Olson
Advisor

Joseph P. Hooper
Co-Advisor

Peter C. Chu
Chair, Department of Oceanography

Oleg A. Godin
Chair, Department of Engineering Acoustics Academic Committee

THIS PAGE INTENTIONALLY LEFT BLANK

ABSTRACT

Detection of underwater explosions by acoustic means, which has been widely researched, is simple, given the large peak pressures produced by these types of sources. By contrast, estimation of the explosive yield and type of explosive by such means has received less attention. This research compares the propagation of acoustic waves in a shallow water waveguide generated by underwater detonations producing broadband impulse signals. Typically, broadband waves are dispersive due to the waveguide in shallow water regions. Data was drawn from experiments conducted near Oahu, Hawai'i, using two explosive sources for different configurations: a conical shaped charge and a standard block. Both sources consisted of Composition C-4 explosive material and were detonated at comparable depths. This thesis focuses on differentiating the propagation of acoustic waves in multiple environments from these two kinds of sources. Simulations were used to explore different seabed properties, which varied by location, and how they impacted peak pressure variability across the Indo-Pacific region. By enhancing the understanding of acoustic propagation of explosive sources in complex environments, this research is helpful in cross domain operations. The developed models can also be applied defensively to determine the optimal placement and number of sensors required to monitor critical infrastructure on the seabed.

THIS PAGE INTENTIONALLY LEFT BLANK

TABLE OF CONTENTS

I. INTRODUCTION....1

II. BACKGROUND....3
A. UNDERWATER ACOUSTICS....3
B. UNDERWATER DETONATION....5

III. EXPERIMENT....11
A. BACKGROUND....11
1. Explosive Sources....11
2. Receivers....12
3. Experiment Design....13
B. FIRST EXPERIMENT....15
C. SECOND EXPERIMENT....22
D. CONICAL SHAPED AND BLOCK EXPLOSIVE SOURCES COMPARISON....28
E. ASSESSING THE DISCREPANCIES USING ACOUSTIC SIMULATION....30

IV. SIMULATIONS IN OTHER ENVIRONMENTS....39
A. SEDIMENT DATA AND BATHYMETRY....39
1. Sediment Physical Properties....39
2. Geoacoustic Properties....40
3. Sediment Information Source....41
4. Justification for Study Sites....41
5. Taiwan Strait....42
6. Philippine Sea....44
7. Luzon Strait....46
8. Qiongzhou Strait....48
9. Malacca Strait....50
B. ACOUSTIC SIMULATION AND RESULTS ACROSS GEOGRAPHIC REGIONS....54

V. SUMMARY AND RECOMMENDATIONS FOR FUTURE WORK....57
A. SUMMARY....57
B. RECOMMENDATIONS FOR FURTHER EXPLORATION....57
C. ENHANCED TECHNIQUES FOR FUTURE WORK....58
1. Time-warping....58

2. Acoustic Simulation with Directional Source.....58
3. Closer Range Experiments.....59

VI. CONCLUSION 61

LIST OF REFERENCES.....63

INITIAL DISTRIBUTION LIST 67

LIST OF FIGURES

Figure 1. Various Types of Sound Propagation Paths in the Ocean. Source [3].....4

Figure 2. Bubble Phase from Explosion and Pressure-Time History. Source: [10].....6

Figure 3. Example of Shock Wave Pressure vs. Time. Source: [10]. 7

Figure 4. Shock Wave Reflections Schematic of Wave Propagation. Source: [10].....8

Figure 5. Pressure History with Bubble Pulses. Source: [10]. 8

Figure 6. Underwater Shock Phenomenology and Bubble Effect. Source [11].....9

Figure 7. Packing C-4 into Shaped Charges.....12

Figure 8. Block of C-4.....12

Figure 9. SM3M Deployment during Experiment (left); SM3M with Box. Source: [14].....13

Figure 10. Weight of Explosive Source vs. Range (left: TNT; right: C-4).....14

Figure 11. Pressure vs. Range of Various Weight of C-4 14

Figure 12. Eight UNDETs Received from Hydrophone#1 (300 m) 16

Figure 13. Eight UNDETs Received from Hydrophone#2 (500 m) 17

Figure 14. Power Spectral Density from Hydrophone#1 (300 m) 18

Figure 15. Power Spectral Density from Hydrophone#2 (500 m) 18

Figure 16. Spectrogram from Hydrophone#1 (300 m).....19

Figure 17. Spectrogram from Hydrophone#2 (500 m).....20

Figure 18. Detonation 10 and Detonation 11 by Time Delay for Hydrophone#1 (300 m).....21

Figure 19. Detonation 10 and Detonation 11 by Time Delay for Hydrophone#2 (500 m).....22

Figure 20. UNDET Sites and Receivers Layout. 24

Figure 21. Eight UNDETs Received from Hydrophone (800 m) 25
Figure 22. Power Spectral Density from Hydrophone#2 (500 m) 25
Figure 23. Spectrogram from Hydrophone (800 m).....26
Figure 24. Detonations 18 and 19 by Time Delay for Hydrophone (800 m) 27
Figure 25. Peak Pressure (Left) and Energy Fluence (Right) vs C-4 Weight 30
Figure 26. Temperature Profile (left); Salinity Profile (right).....31
Figure 27. Density Profile vs. Depth (left); Sound Speed Profile vs. Depth (right) 32
Figure 28. Two Simulated Signals with Two Difference Ranges 33
Figure 29. Simulated Signals Pressure at Receiver 34
Figure 30. Simulated Signals of Detonations 18 and 19 at Frequency Domain 35
Figure 31. Spectrogram of Simulated Signal with 1,150 m Distance 36
Figure 32. Peak Pressure Propagation from Two Cases of Simulation.....37
Figure 33. Left: Ternary Diagram, Based on Sand-Silt-Clay Ratios; Right: Based on Gravel-Sand-Mud Ratios 40
Figure 34. Map of Simulated Locations 42
Figure 35. Taiwan Strait, Based on Bottom Type Database 43
Figure 36. Taiwan Strait Bathymetry Data. Adapted from [31]. 44
Figure 37. Philippine Sea, Based on Bottom Types Database 45
Figure 38. Philippine Sea Bathymetry Data. Adapted from [31]. 45
Figure 39. Luzon Strait, Based on Bottom Types Database 47
Figure 40. Luzon Strait Bathymetry Data. Adapted from [31]. 47
Figure 41. Bottom Topography of the South China Sea. Source: [36]. 48
Figure 42. Qiongzhou Strait, Based on Bottom Type Database 49
Figure 43. Qiongzhou Strait Bathymetry Data. Adapted from [28].....49

Figure 44. Malacca Strait, Based on Bottom Type Database.....51
Figure 45. Malacca Strait Bathymetry Data. Adapted from [28]. 52
Figure 46. Simulated Peak Pressure Map of Five Locations 55
Figure 47. Peak Pressure Variability Across the Indo-Pacific Region.....56

THIS PAGE INTENTIONALLY LEFT BLANK

LIST OF TABLES

Table 1. Sensitivity Values of SM3M.....13

Table 2. Detonation Plan and Results. 15

Table 3. Time Delay Results of Detonations 10 and 11 from 300 m Receiver 21

Table 4. Time Delay Results of Detonations of 10 and 11 from 500 m Receiver 22

Table 5. Detonation Plan and Results 23

Table 6. Time Delay Results of Detonations 18 and 19 from 800 m Receiver. 28

Table 7. Conical Shaped Charge and Block Explosive Sources Comparison 29

Table 8. Input Parameter of Simulation 31

Table 9. Peak Pressure and Energy Fluence from Simulation for Detonations 18 and 19.....34

Table 10. Peak Pressure and Energy Fluence from Experimental Data for Detonation 18 and 19 34

Table 11. Geoacoustic Properties of Continental Shelf and Slope Environments. 41

Table 12. Input Parameters for Simulations of Five Locations. 53

THIS PAGE INTENTIONALLY LEFT BLANK

LIST OF ACRONYMS AND ABBREVIATIONS

A/D	Analog to digital converter
BRI	Belt and Road Initiative
CTD	Conductivity Temperature and Depth
D	Depth of Charge
EOD	Explosive Ordnance Disposal
FSW	Feet Seawater
MDSU	Mobile Diving and Salvage Unit
MSR	Maritime Silk Road
NEW	Net Explosive Weight
OBOR	One Belt One Road Initiative
PE	Parabolic Equation
RAM	Range-dependent Acoustic Model
Sec	Second
SLOC	Sea Lines of Communication
SOFAR	Sound Fixing and Ranging
SRBR	Surface-Reflected Bottom-Reflected
UNDET	Under Water Detonation
UW	Underwater

THIS PAGE INTENTIONALLY LEFT BLANK

ACKNOWLEDGMENTS

I would like to give the most thanks to my two advisors: Professor Derek Olson for advising me on the acoustic theories, simulations, coding, and guidance for this study; and Professor Joseph Hooper for teaching me the fundamental knowledge of shock physics and theory and allowing me to join this great experiment in Hawai'i.

I would also like to thank the following groups and individuals: CDR Paula Travis for her assistance and support for me to finish this thesis for two degrees. Also, my thanks go to CDR Ana Tempone for her great continuous leadership. Professor Chu and Professor Godin, as the two chairs for my curricula, taught me all the required knowledge for this thesis and deserve my sincere appreciation. Mr. Miller has my gratitude for introducing me to the great MATLAB function SM3 read. Mr. Cook, thank you for all assistance on MATLAB problems; thanks also to Dr. Margolina for teaching me about the sediment database, and its MATLAB functions, and for being a really nice officemate; LT Price for his support and for bringing me into this topic of research; LT Harrel for his friendship during my time at the Naval Postgraduate School; LT Green, LT Artabazo, Dr. Mason, and MDSU ONE for their assistance during the experiment in Hawai'i; Dr. Reeder, CDR Shannon, Dr. Hanser, and Mr. Joseph for providing the great equipment for experiment use; LCDR Guarino (Brazilian Navy) for being a real classmate, friend, and mentor on acoustic knowledge; LCDR Well for his advice and encouragement during my time here; LCDR Tsu-Wei Tan (Taiwan Navy) for his simulation and acoustic knowledge; LCDR Garrett, LCDR Rogers, and all my cohort and the Meteorology/Oceanography community for their support. In addition, I am grateful to the Naval Postgraduate School Graduate Writing Center, the Thesis Processing Office, my thesis processer, and my editor for coaching assistance throughout this process. Lastly, there are too many people I should be grateful to, so let me thank God for all good things that happen.

THIS PAGE INTENTIONALLY LEFT BLANK

I. INTRODUCTION

Detection of underwater explosions by acoustic means, which has been the subject of much research, is simple, given the large peak pressures produced by these types of sources. By contrast, estimation of the explosive yield and type of explosive by such means has received less attention. This paper aims to narrow that gap in the research by studying the propagation of acoustic waves in a shallow water waveguide generated by underwater detonations producing broadband impulse signals. Our data analysis draws on field experiments conducted at Pu'uloa Underwater Detonation Range off the coast of Oahu, Hawai'i. The configurations studied here are determined by two sources: 1) a standard block explosive and 2) a conical shaped charge. Both consist of Composition C-4 explosive material and were detonated at comparable depths. These two explosive types are fairly commonly used for experiments conducted in naval and commercial operations [1], [2].

The primary motivation of this research was to determine whether the received acoustic signal depends on the source type and/or its weight, and then to test whether that knowledge could be used to determine the type of explosive source. Typically, broadband waves are dispersive due to the waveguide in shallow water regions, and this acoustic dispersion complicates identification of the signal's source when the receiver is distant from the source. Hence, this thesis focuses on differentiating propagation of acoustic waves in multiple environments from the two types of sources used in the field experiments.

The results and analysis of these experiments are based on modeling using the parabolic equation acoustic model in a shallow waveguide to simulate different seabed properties according to location and peak pressure variability across the Indo-Pacific region. Other types of environments of areas of naval interest in the Indo-Pacific region were studied by using the acoustic model with parameters gathered from database information. Thus, as the research aims to enhance our understanding of acoustic propagation of explosive sources in complex environments, it will be helpful in cross domain operations. Moreover, these models could be applied defensively to determine

optimal placement and number of sensors required to monitor critical infrastructure on the seabed.

This research spans six chapters. Chapter II provides background information on both underwater acoustics and shock waves. Chapter III details the experiments that were conducted, and presents an analysis of shock wave measurements as a function of source type and weight. Further, in Chapter IV, we study the effect of varying the environmental properties on the peak pressure of shock waves in shallow water. Discussion is presented in Chapter V, followed by conclusions from this research, which are summarized in Chapter VI.

II. BACKGROUND

This chapter provides basic background material that serves as the foundation for this research. Two main disciplines are applied in this research, underwater acoustics and underwater explosion physics, which includes the formation of shock waves as well as explosive wave propagations in an aquatic environment.

A. UNDERWATER ACOUSTICS

Underwater sound is directly impacted by the ocean environment, which is defined as the water column bounded above by the water surface and below by the sea floor. One of the dominant factors in the water column is the speed of sound, which is directly impacted by temperature, static pressure, and salinity. Sound speed in the ocean is represented by an increasing function that is respective to the three variables: temperatures, static pressure, salinity and with a function of depth.

Sound can have various propagation paths in the ocean depending on the surrounding environment. Figure 1 provides an example as the simplest schematic of the common types of sound propagation in the ocean. Rays can interact with the surface only, as they do in paths A, B, and D in the figure. Rays can also interact with the ocean interior and never intersect the ocean surface, as in path C. Path F illustrates rays reflected off both the ocean surface and the seabed, which is referred to as surface-reflected bottom-reflected (SRBR) rays [3]. The variation in ocean properties with range adds complexity when modeling sound propagation .

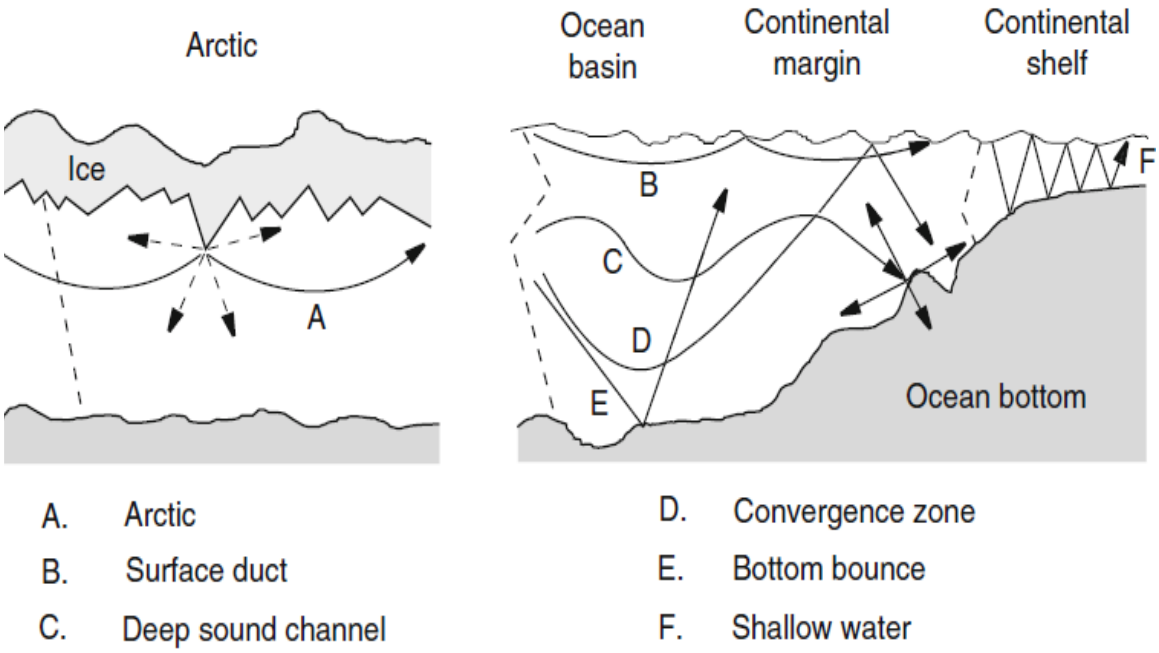

Figure 1. Various Types of Sound Propagation Paths in the Ocean. Source [3].

Sound in shallow water regions, the primary focus of this research, interacts with both the ocean surface and sea floor. In such regions, a significant characteristic of sound propagation is that the sound speed profile is mostly constant over depth. Also, sound interacts many times with the ocean bottom, the properties of which strongly affect the signal at a distant receiver.

One common method to describe wave propagation is to use parabolic approximations for wave equations [4], [5]. The history of "parabolic wave equations (PE) goes back to the mid-1940s when Leontovich and Fock applied a PE method to the problem of radio wave propagation in the atmosphere" [6]. After the work of those researchers, parabolic equations were adopted in several fields of science including underwater acoustics, seismic geophysics, optics, and medical ultrasonic [7]. PE methods are particularly useful for solving range-dependent wave propagation problems when scattering is negligible.

This derivation follows the development presented in [5]. The standard PE derivation starts with a time harmonic acoustic field in a cylindrical coordinate system (r, z, ϕ).

$$\mathrm{P(r,z,\phi,\omega t) = p(r,z,\phi)e^{-i\omega t}}. \tag{2.1}$$

Most of the range-dependence of pressure can be captured using cylindrical spreading, and so the variable $\psi(r, z, \phi)$ is used here instead. The auxiliary pressure $\psi(r, z, \phi)$ is defined as,

$$\mathrm{P(r,z,\phi) = \psi(r,z,\phi)H_0{}^{(1)}(K_0 r)}. \tag{2.2}$$

Substituting the previous equation into the Helmholtz equation results in

$$\frac{\partial^2 \psi}{\partial r^2} + 2iK_0 \frac{\partial \psi}{\partial r} + \frac{1}{r^2}\frac{\partial^2 \psi}{\partial \phi^2} + \frac{\partial^2 \psi}{\partial z^2} + K_0{}^2 \left(n^2 - 1 + \frac{1}{4K_0{}^2 r^2}\right)\psi = 0. \tag{2.3}$$

Here the $K_0 = \frac{\omega}{c}$, K_0 is the reference wavenumber and $n(r, z, \phi) = \frac{c_0}{c(r,z,\phi)}$, where n is the acoustic index of refraction. Using a small angle approximation, this can be simplified to the standard PE result [8]:

$$\frac{\partial \psi}{\partial r} = \frac{i}{2K_0}\frac{\partial^2 \psi}{\partial Z^2} + \frac{iK_0}{2}(n^2 - 1)\psi\,. \tag{2.4}$$

B. UNDERWATER DETONATION

Underwater explosions are caused by a rapid expansion of gas due to a chemical reaction [9], [10]. Underwater explosions consist of two distinct loading phenomena, a high frequency shock wave, which is generated from the detonation of the explosive material, and a low frequency pulsating bubble from the explosive gas. Figure 2 shows the exponential decay of pressure from the explosion and the phase of gas bubble during the entire explosion.

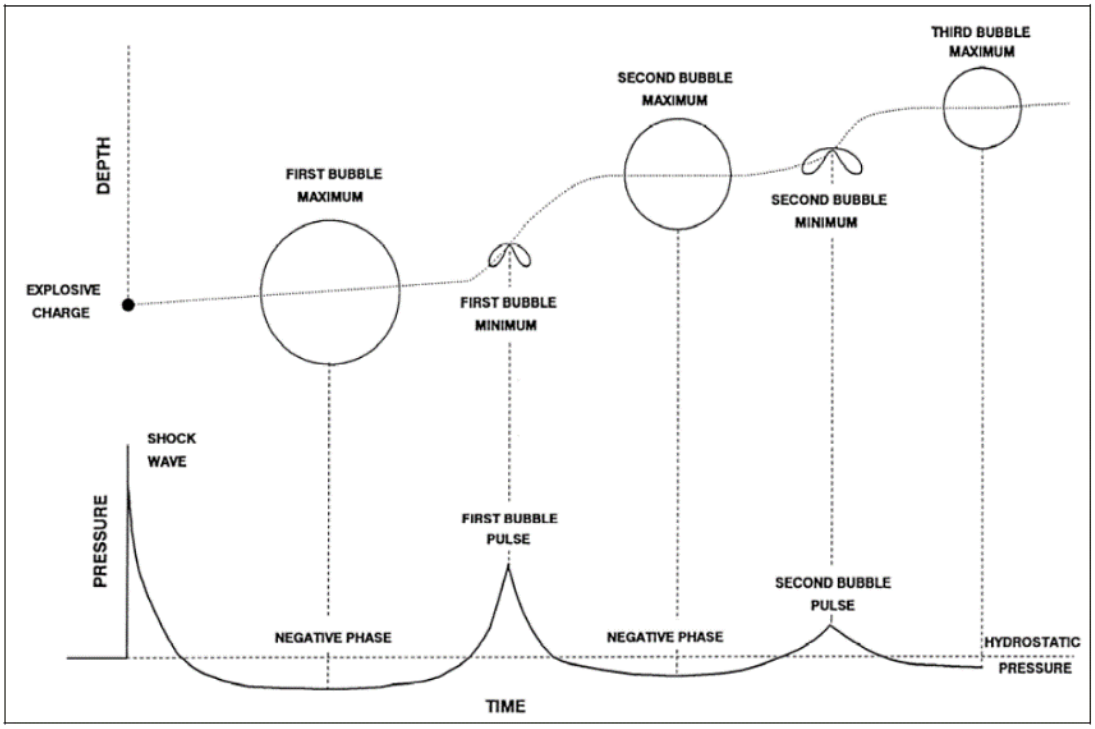

Figure 2. Bubble Phase from Explosion and Pressure-Time History.
Source: [10].

The scaling laws for early formulation were developed at the Naval Ordnance Lab at White Oak [11]. The shock pressure $P(t)$ in Equation (2.16) decays exponentially after the initial dynamic loading of the fluid medium.

$$\mathrm{P(t)} = \mathrm{P_{max}} \mathrm{e}^{(-\frac{\mathrm{t}}{\theta})} \tag{2.5}$$

The shock wave pressure from an underwater explosion experiment appears in Figure 3.

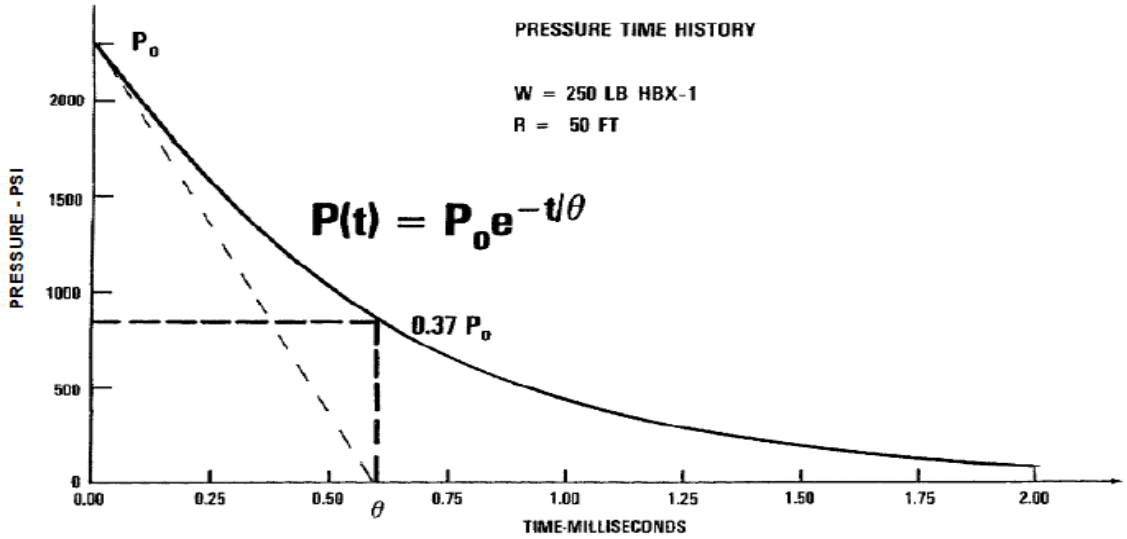

Figure 3. Example of Shock Wave Pressure vs. Time. Source: [10].

The shock wave pressure depicted in Figure 3 is drawn from an underwater explosion experiment using a TNT weight of 113.4 kg, measured at a distance of 15.24 m. It confirms that the pressure of the detonation decays approximately exponentially. To determine P_{max} , it is common to use scaling laws and experiment to relate it to the mass of the explosive [11],

$$P_{max} = 52.4\left(\frac{W^{\frac{1}{3}}}{R}\right)^{1.18}, \tag{2.6}$$

where W in Equation (2.6) is the TNT equivalent mass of the underwater explosive in kilograms. The TNT equivalent equals the mass of C-4 times 1.34.

In the ocean, a source interacts with ocean boundaries many times before arriving at a receiver. Figure 4 illustrates such an interaction in the medium field, which is many charge diameters away, but each path can be clearly distinguished. At longer ranges, these paths cannot be distinguished, and waveguide dispersion is more evident.

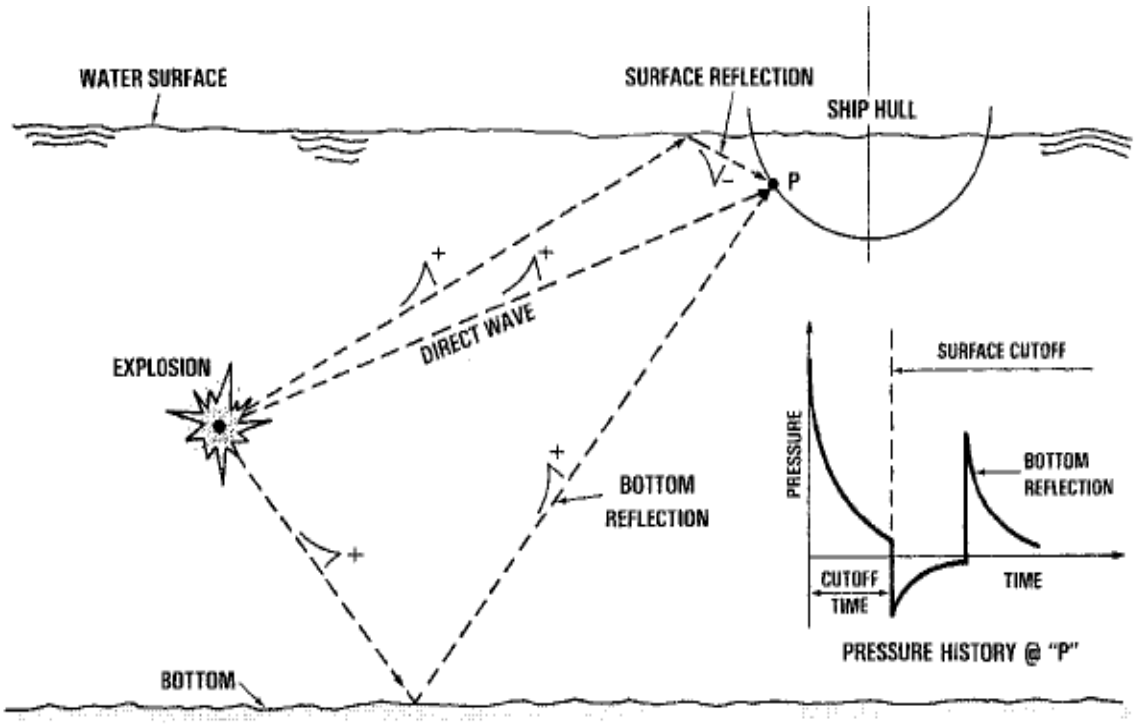

Figure 4. Shock Wave Reflections Schematic of Wave Propagation. Source: [10]

After the initial shock, a bubble is formed then later collapses. This is called the bubble pulse. The bubble pulse plays an integral part during the entire explosive cycle. Figure 5 gives an example of bubble pulses caused by bubbles collapsing from an experiment [12].

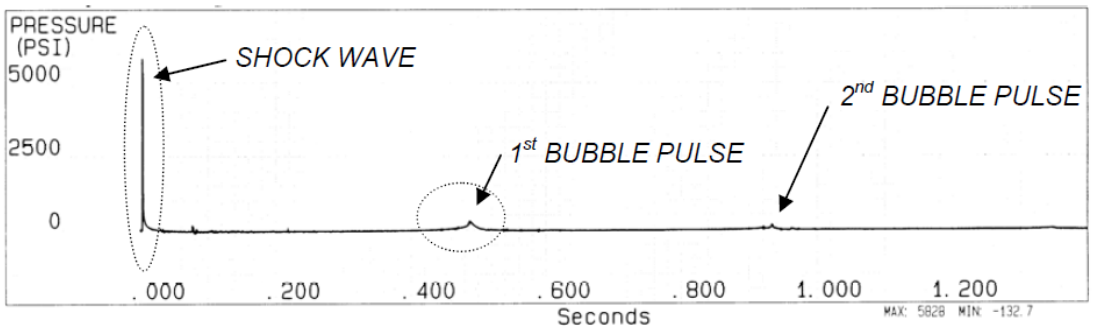

Figure 5. Pressure History with Bubble Pulses. Source: [10].

The bubble pulse time delay is the duration between the initial shock and the first bubble collapse. This time has been calculated from scaling laws and experiments [11],

$$T = 2.08 * \frac{W^{\frac{1}{3}}}{(D+10)^{\frac{5}{6}}}. \tag{2.7}$$

In Equation (2.7) [11] T is the time delay from the first full oscillation. This cycle from first burst, full expansion, and back to the first minimum is depicted in Figure 6. Here, T is delay time with unit in seconds, and D is the depth with unit in meters. Furthermore, the maximum radius is expressed as Equation (2.8) [11]

$$a_{MAX} = 3.3 * (\frac{W}{D+10})^{\frac{1}{3}}, \tag{2.8}$$

where the unit of a_{MAX} is dependent on depth D.

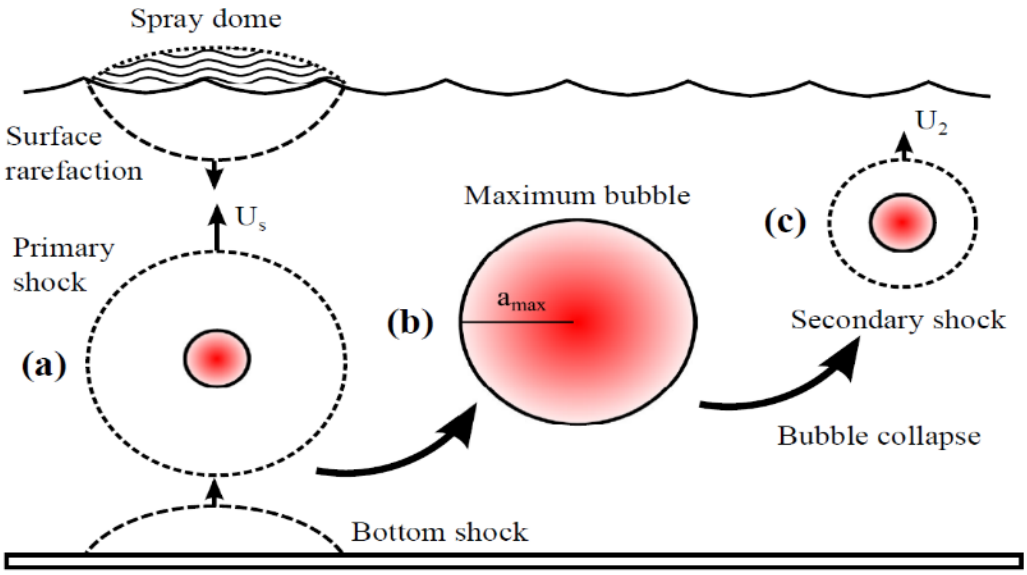

Figure 6. Underwater Shock Phenomenology and Bubble Effect. Source [11].

THIS PAGE INTENTIONALLY LEFT BLANK

III. EXPERIMENT

A. BACKGROUND

Two field experiments were performed at an underwater detonation site off the coast of Oahu, Hawai'i. Materiel and personnel support were provided by Mobile Diving and Salvage Unit (MDSU) ONE, U.S. Navy, which provided diving, demolition, and small craft support. Explosions were conducted in two locations, one on a nearby land demolition range and another on an underwater range. For the purposes of this study, only the underwater experiments are analyzed. Operations in both locations were performed by MDSU ONE's personnel who are certified in handling and detonating live explosives.

1. Explosive Sources

The source used for both field experiments consisted of C-4 explosives. Two shapes of materiel were employed: conical shaped charges with a copper liner (shown in Figure 7) and a block of C-4 (shown in Figure 8). The mass of C-4 in the net explosive weight (NEW) required conversion to equivalent TNT for use in the formulas given in Chapter II. The NEW for a block of C-4 is 567g (1.25 lbs).

The C-4 was cut into pieces in non-uniform shapes and packed into plastic containers encircled with copper wires. This step is important because it can help achieve required material properties and penetration through a desired metal target from explosive sources.

Figure 7. Packing C-4 into Shaped Charges

Figure 8. Block of C-4

2. Receivers

The primary hydrophones used in both experiments were the *Song Meter Submersible and Deep Water Bioacoustics Recorder* (SM3M) manufactured by Wildlife Acoustics, Inc [13]. Figure 9 shows the appearance of the SM3M. Two SM3M hydrophones were deployed during each experiment. Each hydrophone had two receivers with different sensitivities, and each receiver could gather low or high amplitude acoustic data, depending on the receiver's sensitivity value (see Table 1).

Table 1. Sensitivity Values of SM3M

# Hydrophone	Sensitivity Layout	Sensitivity Values (Low; High) dB re:1V/µPa
#1	LS; HS	164.7; 240.4
#2	HS; LS	164.2; 239.8

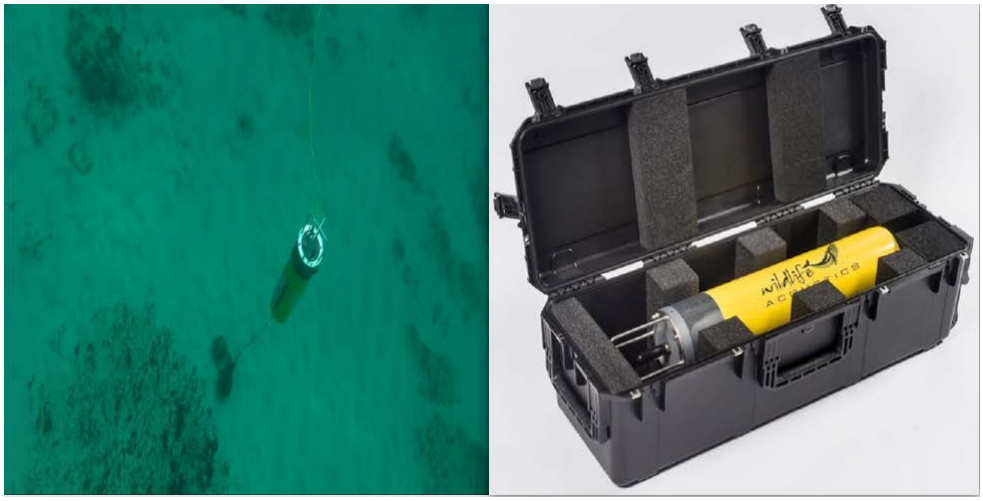

Figure 9. SM3M Deployment during Experiment (left); SM3M with Box. Source: [14].

3. Experiment Design

In the design of the experiment, one aspect considered was the range that the hydrophone was placed from the source. The ideal distance for analyzing acoustic characteristics of explosive sources is as close to the source as possible without damaging the receivers. Otherwise, the effects of waveguide propagation distort the received signal. The receiver cannot be too close to the source, however, because the receiver electronics would clip the signal and distort the signal even more. To determine the ideal location for the source, two variables were considered: sensitivity values and the mass of C-4. Therefore, some calculations were done to determine the receiver locations. Shock wave scaling laws [11], the weight of C-4, and the hydrophone sensitivity were combined to result in Figure 10, which shows the relationship between the peak pressure from the explosive source versus range in meters. Figure 11 gives an idea on how to adjust the

distance between the source and the range. With the 180 and 220 dB re V/1 µPa as the ideal pressure levels from the explosive source, the corresponding range can be calculated. The corresponding ranges were 300 m and 500 m for the first field test in order to obtain the received signal around 210 dB re V/1 µPa to avoid clipping. Moreover, the range of the second experiment was around 800 m, to allow for the flexibility to use larger explosive weights, and therefore larger peak pressures.

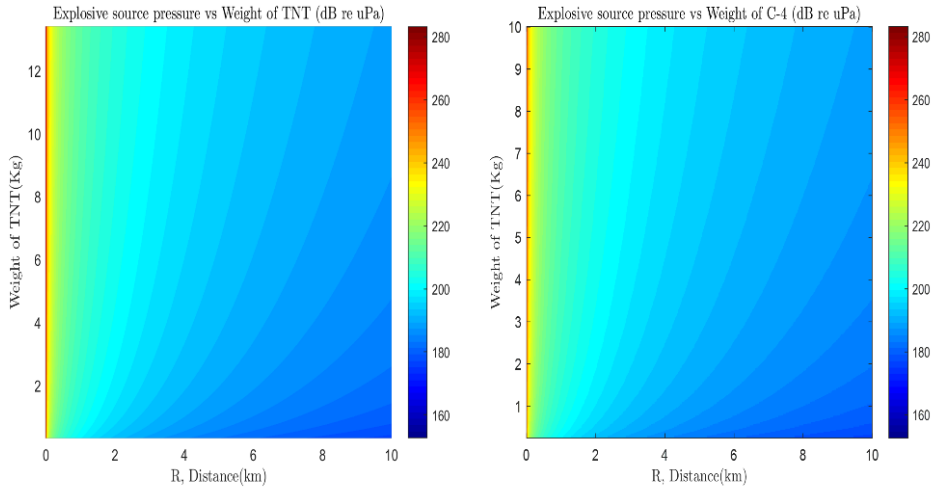
Explosive source pressure vs Weight of TNT (dB re uPa)
Weight of TNT(Kg)
R, Distance(km)
Explosive source pressure vs Weight of C-4 (dB re uPa)
Weight of TNT(Kg)
R, Distance(km)

Figure 10. Weight of Explosive Source vs. Range (left: TNT; right: C-4)

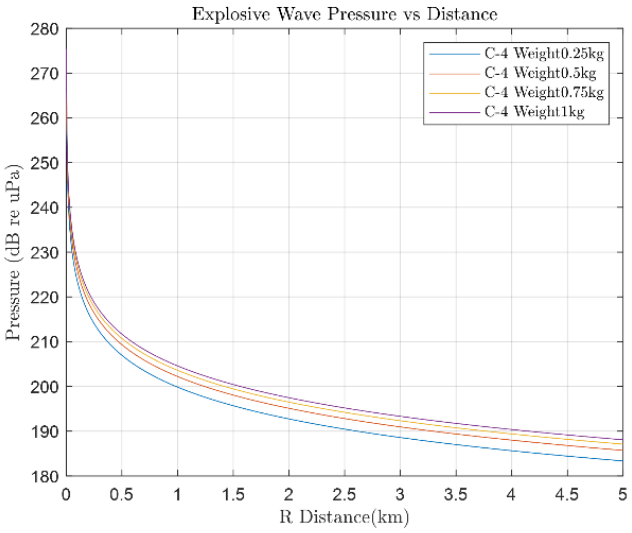

Figure 11. Pressure vs. Range of Various Weight of C-4

B. FIRST EXPERIMENT

The first experiment took place between 15 and 19 April 2019, off the coast of Oahu, Hawai'i. There were 11 shots total from the first experiment. These 11 shots included three land detonations on day one and eight underwater detonations (UNDET) throughout the remainder of the week. The detonation plan of this trip displays as Table 2.

Table 2. Detonation Plan and Results.

Date (2019)	Det #	Site. Depth [fsw]	C-4 [g]	Data - Sheet [g]
15 APR	1	Land	201	36
	2		197	32
	3		213	31
16 APR	4	UW 30	214	29
17 APR	5		215	35
	6		209	34
	7(D)		215	29
	8(D)		196	33
18 APR	9(D)	UW 32	226	31
	10(D) (C-4 only)		567	0
	11 (C-4 only)		569	0

Prepared by: LT Chris Price, LT Wei-Ming (Andy) Chiu
UW = Underwater; fsw = feet seawater; D = Double detonations with few seconds

As the detonation plan shows, there were three days of underwater detonations for each experiment. The depth at the detonation site on 16 and 17 April was 30 feet (9.144 meters), and the detonation depth on 18 April was 32 feet (9.754 meters).

There were eight underwater detonations in all from the April experiment. There were two UNDETs with a block of C-4, which were UNDETs 10 and 11, and the remaining detonations were with a conical shaped charge. In each detonation, the main pulse from the explosion was clearly displayed. Then, many late arrivals showed up following the first peak. Also, each detonation included both huge positive and negative pressure in a very short time.

The time-domain signals from the receivers at 300 meters and 500 meters, respectively, are shown in Figures 12 and 13, and the power spectral density from those two receivers is presented in Figures 14 and 15.

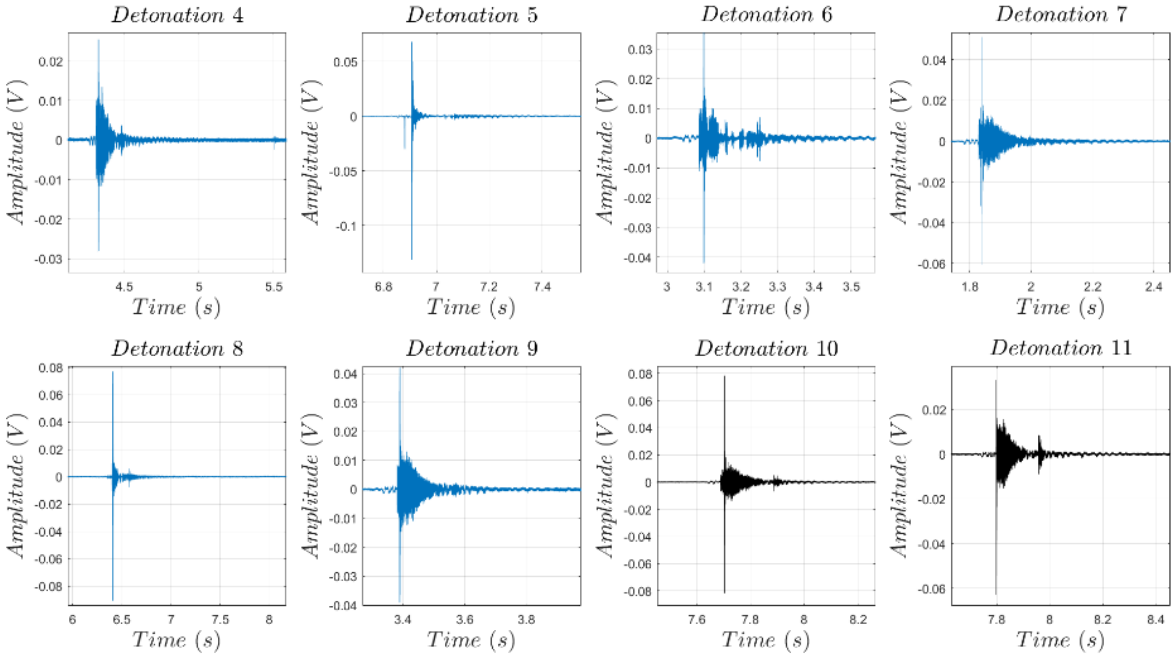

Blue curve is detonation from conical shaped charge, black curve is detonation from Block of C-4.

Figure 12. Eight UNDETs Received from Hydrophone#1 (300 m)

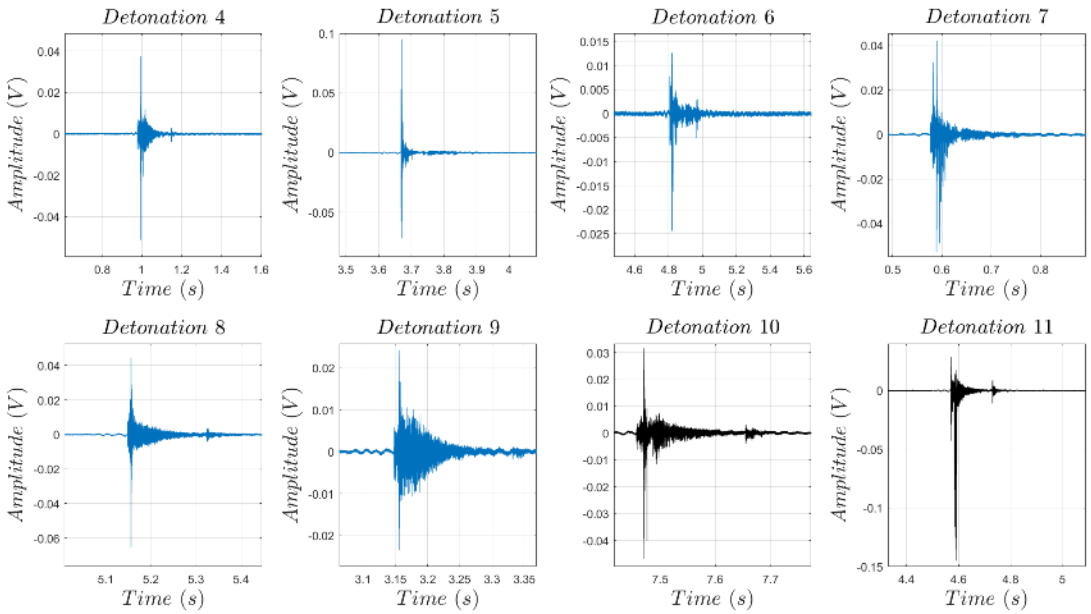

Blue curve is detonation from conical shaped charge, black curve is detonation from Block of C-4.

Figure 13. Eight UNDETs Received from Hydrophone#2 (500 m)

Both Figures 14 and 15 show the power spectral density without averaging (blue and black curves) and with averaging (red curve). The blue curve denotes conical shaped charges, and the black curve is the block charge for all eight detonations from the 300-meter range receiver.

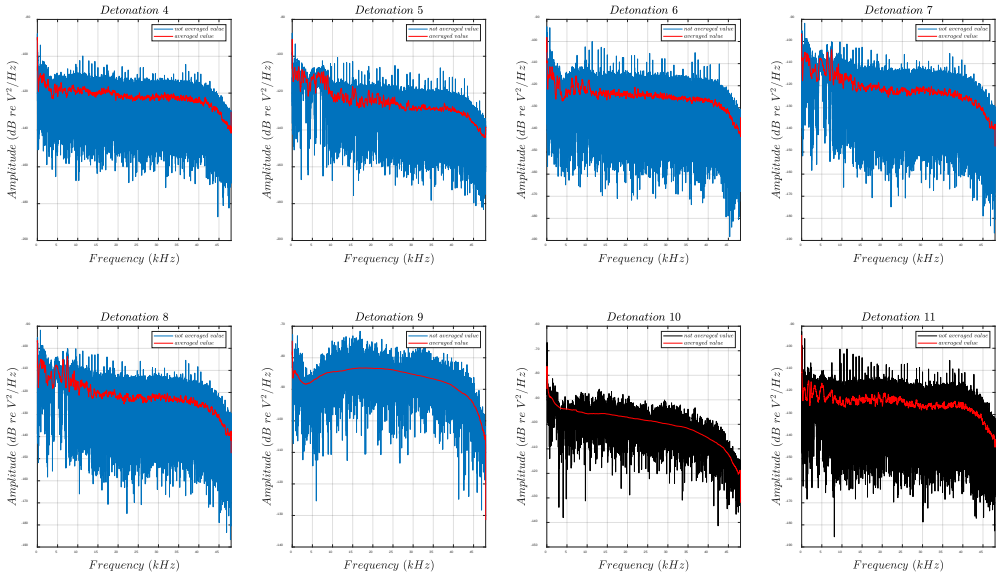

Blue curve is the not averaged value of conical shaped charge detonations, black curve is the not averaged value of block of C-4 detonation, and red is its average value for all detonations.

Figure 14. Power Spectral Density from Hydrophone#1 (300 m)

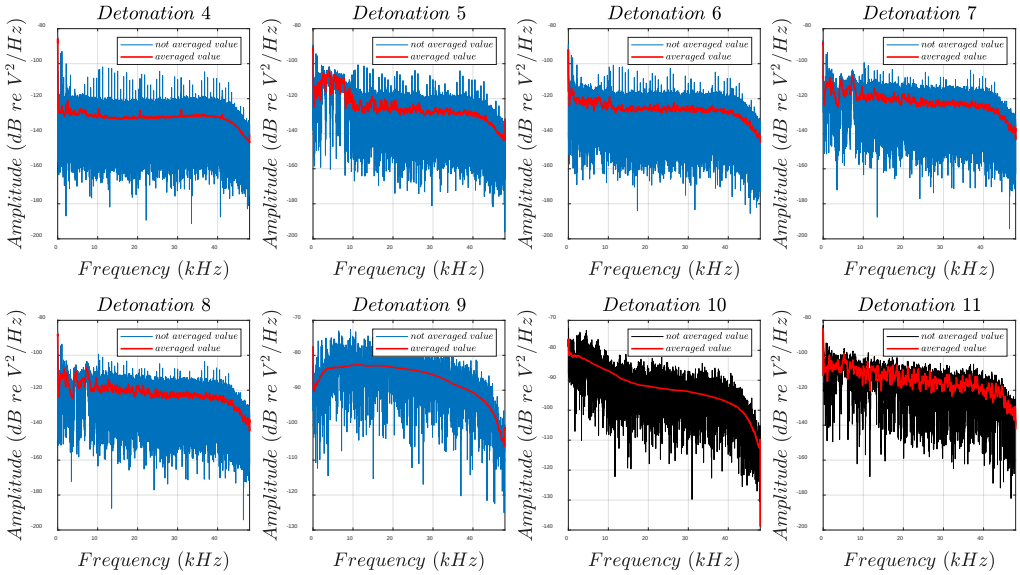

Blue curve is the not averaged value of conical shaped charge detonations, black curve is the not averaged value of block of C-4 detonation, and red is its average value for all detonations.

Figure 15. Power Spectral Density from Hydrophone#2 (500 m)

The sample frequency of the hydrophone analog to digital converter (A/D) is 96 kHz, and the range on the frequency domain is from 0 Hz to 48 kHz. Figures 14 and 15 illustrate that every detonation was a broadband signal. Most of the shapes contain a peak at low frequencies and a relatively flat portion at higher frequencies. However, the low frequency peak is sometimes absent, as in detonation 9 of Figure 15.

Figures 16 and 17 are the spectrograms of all detonations from two different ranges of hydrophones back to the first experiment. The strength of the received signals of all detonations can be recognized from the first figure of the two hydrophones located at different distances. There were six harmonic signals across the entire time, with three of them happening around 1030, 2060, and 3090 Hz, and the rest of the three at approximately 10, 20, and 30 kHz, respectively. These signals may be electronic noise from the SM3M. The detonations from the conical shaped charges seem to have relatively stronger energy presenting on the low frequency spectrum (0–10 kHz band). On the other hand, the detonations from a block of C-4 show broadband energy across much of the frequency spectrum. Detonation 11 was the best example of this.

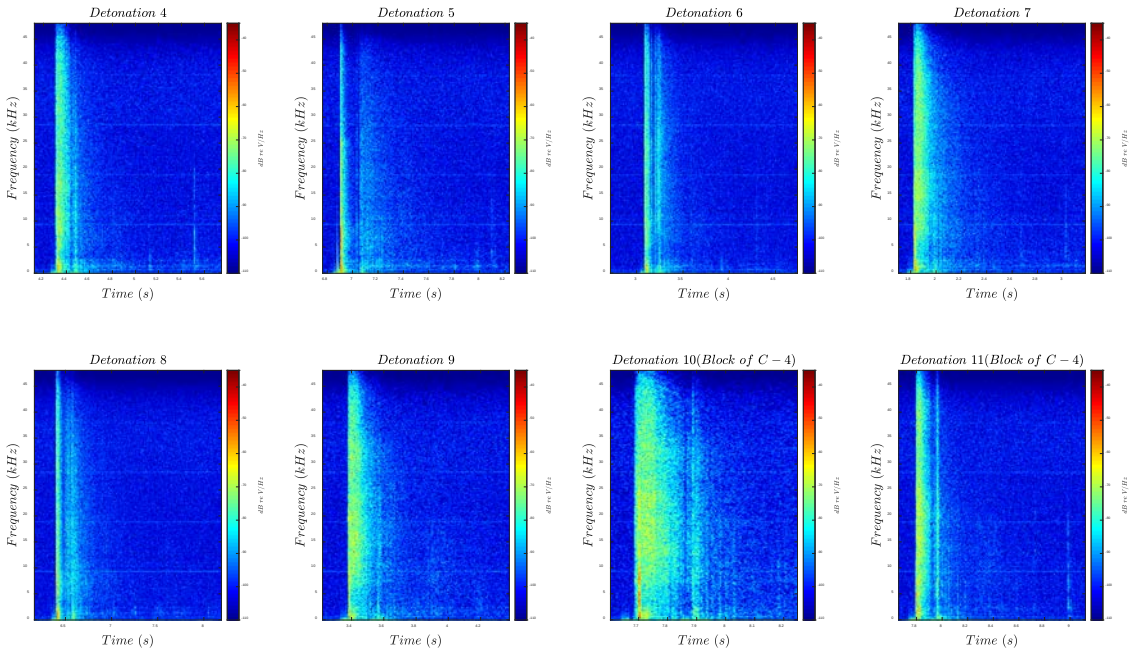

Figure 16. Spectrogram from Hydrophone#1 (300 m)

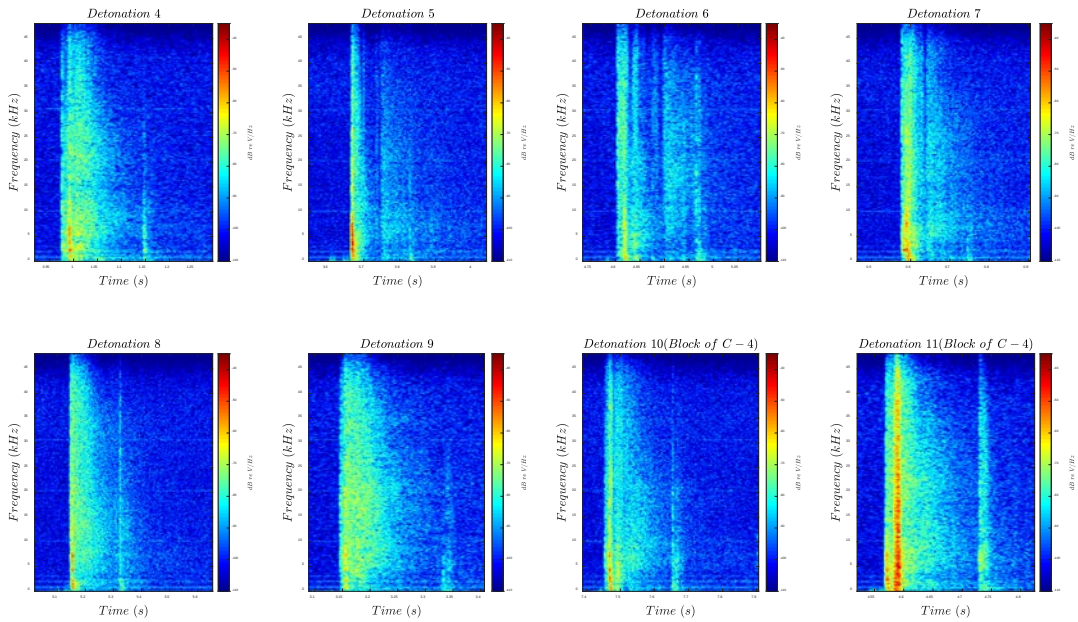

Figure 17. Spectrogram from Hydrophone#2 (500 m)

In order to calculate the time from the primary shock to the second shock right after the bubble collapses, we assess when the two peak pressure spikes occur in the data. After reviewing all signals in the time domain, the primary peak and secondary peak were more identifiable for the block of C-4, which was from detonations 10 and 11, than from the shaped charges. These experimental measurements of time delay are compared with Equation (2.18). As the results in Table 3 (300-meter range receiver) and Table 4 (500-meter range receiver) show, detonation 10 has a greater percentage error than detonation 11. The potential reason for this is detonation 10 was the second detonation, followed a few seconds later by detonation 9, and the water may have had residual microbubbles. Detonation 11 was just a single blast by itself. So a potential explanation for the bubble pulse delay discrepancy may be that the explosion was altered by the increased compressibility of the water by detonation 9. Furthermore, those two detonations have almost the same predicted maximum bubble radius due to their identical source depth.

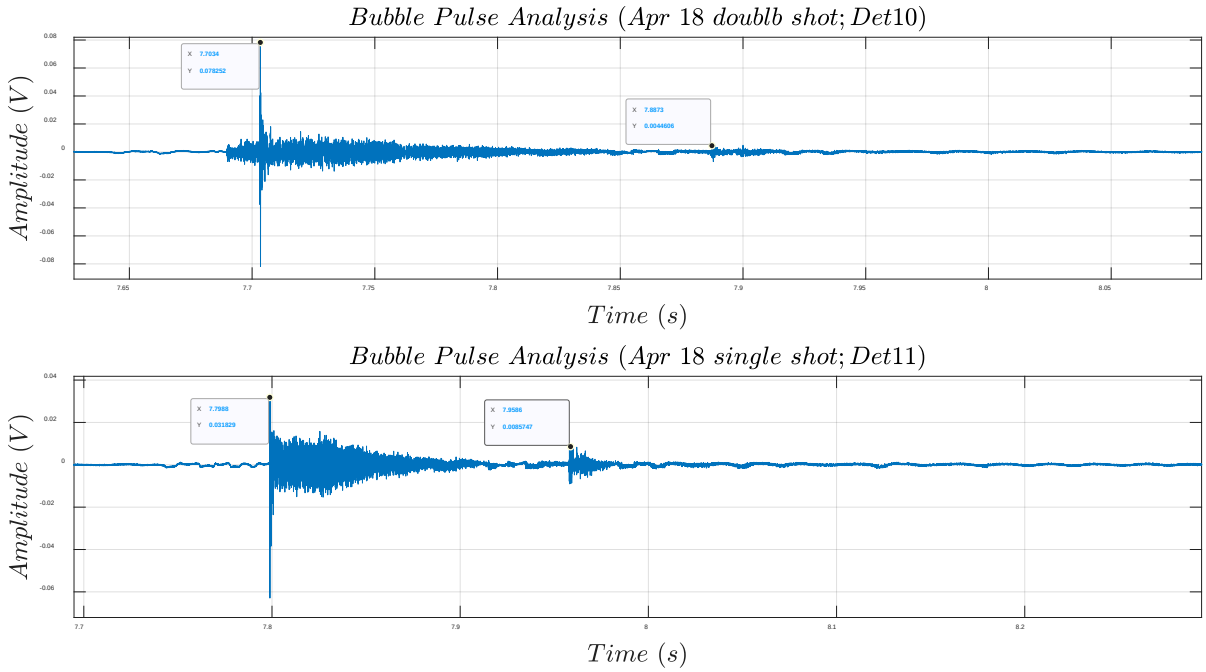
Bubble Pulse Analysis (Apr 18 doublb shot; Det10)
Amplitude (V)
Time (s)
Bubble Pulse Analysis (Apr 18 single shot; Det11)
Amplitude (V)
Time (s)

Figure 18. Detonation 10 and Detonation 11 by Time Delay for Hydrophone#1 (300 m)

Table 3. Time Delay Results of Detonations 10 and 11 from 300 m Receiver

Detonations (300 m receiver)	Theoretical Delay Time (S)	Experimental Delay Time (S)	Percentage Error (%)	Maximum Bubble Radius (m)
#10 (567 g of C-4)	0.1622	0.1839	13.38	3.6930
#11(569 g of C-4)	0.1623	0.1591	2.01	3.6974

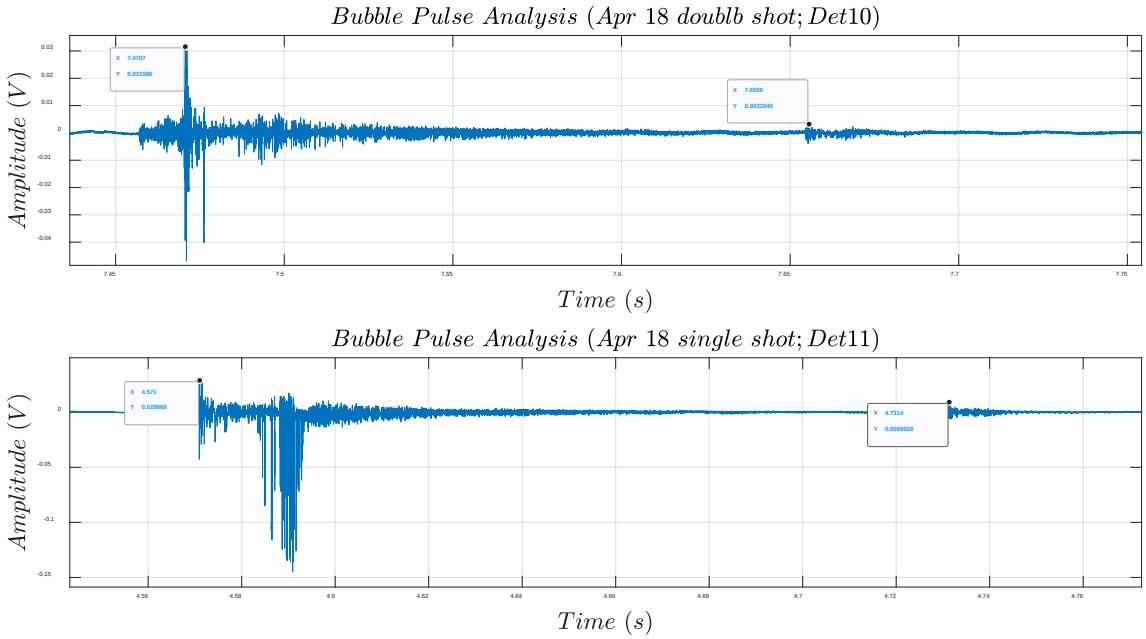
Bubble Pulse Analysis (Apr 18 doublb shot; Det10)
Amplitude (V)
Time (s)
Bubble Pulse Analysis (Apr 18 single shot; Det11)
Amplitude (V)
Time (s)

Figure 19. Detonation 10 and Detonation 11 by Time Delay for Hydrophone#2 (500 m)

Table 4. Time Delay Results of Detonations of 10 and 11 from 500 m Receiver

Detonations (500 m receiver) (source depth 9.1m)	Theoretical Delay Time (S)	Experimental Delay Time (S)	Percentage Error (%)	Maximum Bubble Radius (m)
#10 (567 g of C-4)	0.1622	0.1838	13.38	3.6930
#11(569 g of C-4)	0.1623	0.1604	1.18	3.6974

C. SECOND EXPERIMENT

The second experiment took place between 18 and 22 November 2019 in the same location as the first experiment. There were 10 shots in total, with two land shots on day one and eight UNDETs throughout the rest of the week. The detonation plan of this experiment is shown in Table 5.

Table 5. Detonation Plan and Results

Date (2019)	Det #	Site. Depth [fsw]	C-4 [g]	Data - Sheet [g]
19 NOV	12	UW 45	176.0	15
	13		170.3	14
	14(D)		170.7	14
	15(D)		175.9	14
20 NOV	16	UW45	170.2	16
	17		176.0	13
	18(D) (C-4 only)	UW45	590	0
	19(D) (C-4 only)	UW 60-70	593	0
21 NOV	20	Land	176.5	14
	21		176.5	14
Prepared by: LT Chris Price, LT Wei-Ming (Andy) Chiu UW = Underwater; fsw = feet seawater; D = Double detonations with few seconds				

As noted previously, the distance between the source and the receiver was different in the second experiment. We placed the receiver further from the source for the second experiment so that a larger distance was used to allow for the possibility of detonating much larger blocks of C-4. The actual weights, however, were not much more than in the first experiment. The team deployed two SM3M hydrophones as before, with one located around 800 meters from the source and another one located 500 meters from the source. Another two Acousonde [15] hydrophones were deployed north (shoreside) of the detonation site and another one deployed south (seaside). Unfortunately, one SM3M and one Acousonde were lost during the experiment. The surviving Acousonde did not activate and no data was recorded. Thus, the only data from the second experiment was from one SM3M located at 800 meters from the source and with a depth of 15 meters.

In the second trip a conductivity, temperature, depth sensor (CTD) was used to measure the sound speed profile. The water depth of the receiver's location was obtained from the CTD and was measured as 17.47 meters. The receiver depth was calculated around 15 meters since there was a 6–8 foot line connecting the receiver package and the mooring weight. Additionally, detonation 19, which was the last explosion conducted on the last day was about 250 meters east and five meters deeper than other detonations due

to a stronger wind that blew from the west. Figure 20 gives the picture of the layout of the underwater detonation site and the receivers.

Figure 20. UNDET Sites and Receivers Layout.

Detonations from Conical Shaped Charge and Block of C-4

a. Time Domain Signal

The procedure for this experiment was the same as it was for the previous test. Shot numbers 18 and 19 used a block of C-4 while the rest of the detonations were from a conical shaped charge. Again, the main pulse is visible from the time-domain measurement as presented in Figure 21. Some samples seem to have several late arrivals after the signal's primary peak, which are likely from bubble collapse.

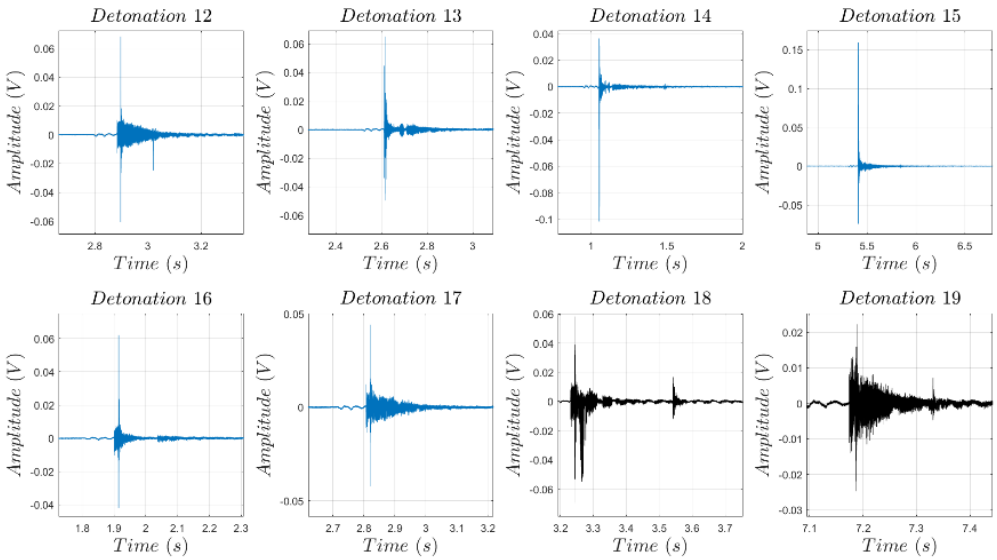

Blue curve is detonation from conical shaped charge; black curve is detonation from Block of C-4.

Figure 21. Eight UNDETs Received from Hydrophone (800 m)

The power spectral density from the second experiment is shown in Figure 22.

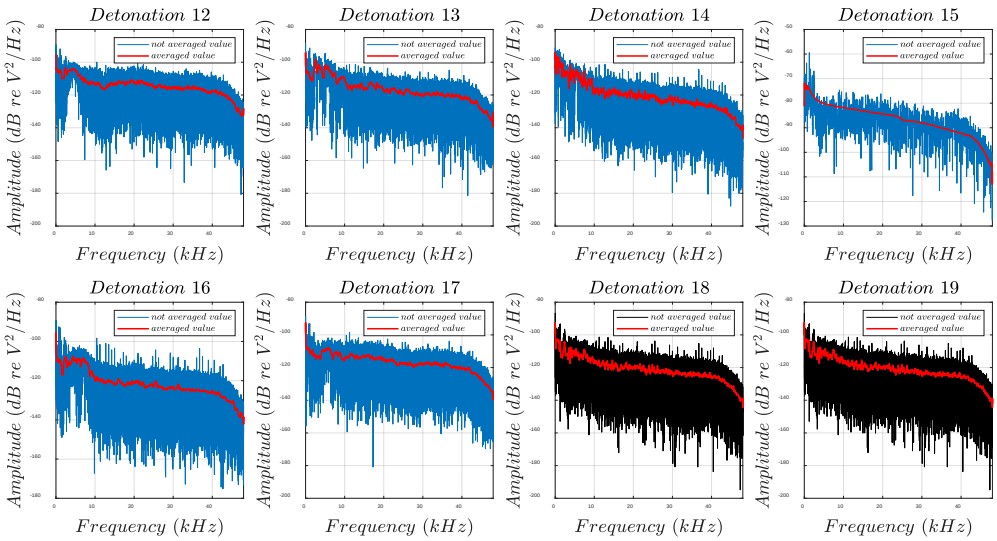

Blue curve is the not averaged value of conical shaped charge detonations, black curve is the not averaged value of block of C-4 detonation, and red is its average value for all detonations.

Figure 22. Power Spectral Density from Hydrophone#2 (500 m)

As can be seen in Figure 22, the frequency axis ranges from 0 Hz to 48 kHz, which is the Nyquist frequency for this instrument. The blue curve denotes conical shaped charges without averaging, the black curve denotes block C-4 detonations without averaging, and the red curve denotes the spectrum calculated using averaging for both types of sources. Interestingly, the two detonations from the block of C-4 have very similar representation in the frequency domain, but appear totally different in the time domain. Also, the detonations from the block of C-4 seem to have a more stable amplitude compared with the conical shaped charge detonations. Again, most of the power spectral densities have a peak at low frequencies and a relatively flat portion between about 10 kHz and 30 kHz. After 40 kHz, the spectra begin to taper off due to the anti-aliasing filter of the SM3M.

Following with the same step from the previous experiment, the eight subplots in Figure 23 show spectrograms of the eight detonations. The horizontal lines are at the same frequencies as in the first experiment and support the hypothesis that they are from electronic noise from the instrument. Some of the detonation signals are very spread out in time (detonations 12, 17, and 19) and some are very short (detonation 18).

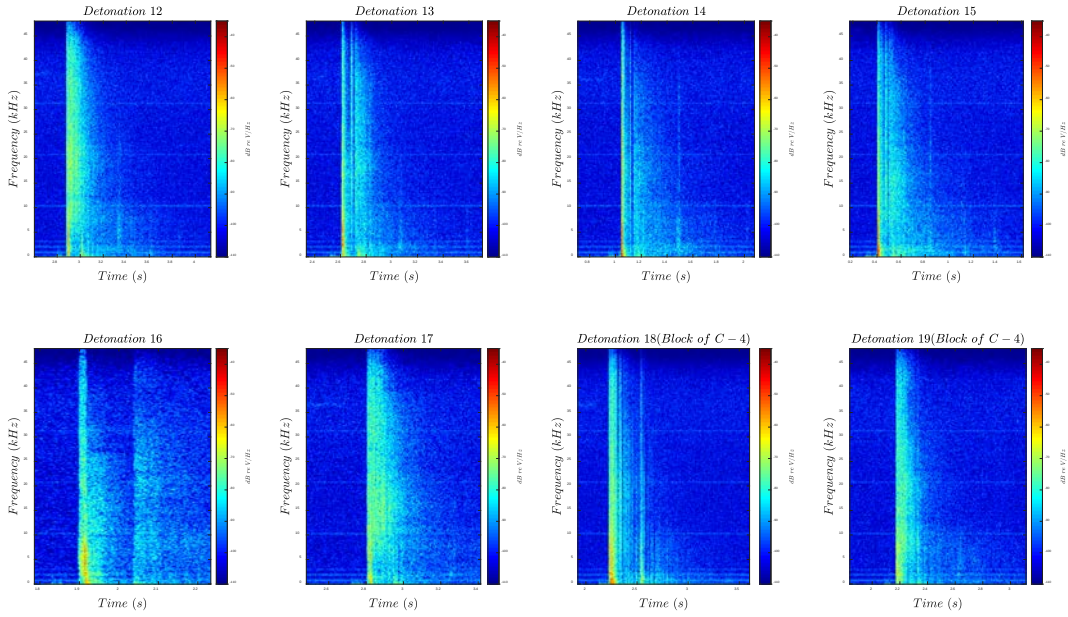

Figure 23. Spectrogram from Hydrophone (800 m)

Repeating the same procedures from the first experiment to calculate the time from the primary shock to the second shock right after the bubble collapses, we assess when the two peak pressure spikes occur in the data. After reviewing all signals in the time domain, we found the primary peak and secondary peak were more identifiable for the block of C-4, from detonations 18 and 19. These experimental measurements of time delay are compared with Equation (2.18). Table 6 shows the results for the time delay and the maximum bubble radius for those two detonations. Detonation 18 has a large error of percentage of error (55.05 %), while detonation 19 has a smaller percentage of error (5.47 %). The potential reason for this error difference could be because of the location of the detonation. Detonation 19 was measured with a greater range and detonated at a deeper depth than detonation 18. Both detonations were double detonations, meaning that two explosions were triggered in a short amount of time (within a few seconds). The residual microbubble field from previous explosions may have caused this significant variation in the bubble pulse time.

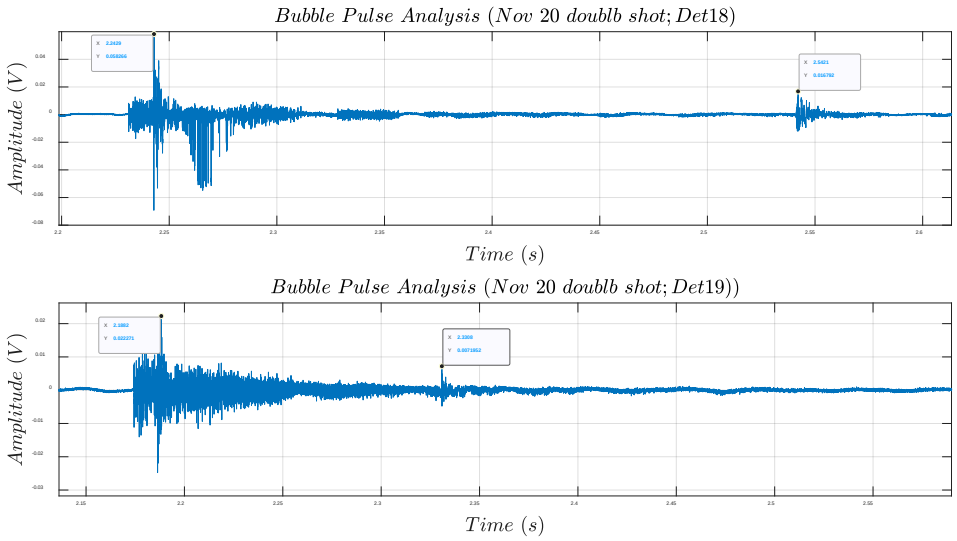
Bubble Pulse Analysis (Nov 20 doublb shot; Det18)
Amplitude (V)
Time (s)
Bubble Pulse Analysis (Nov 20 doublb shot; Det19))
Amplitude (V)
Time (s)

Figure 24. Detonations 18 and 19 by Time Delay for Hydrophone (800 m)

Table 6. Time Delay Results of Detonations 18 and 19 from 800 m Receiver.

Detonations (# 18 800 m receiver) (# 19 1050 m receiver)	Theoretical Delay Time (S)	Experimental Delay Time (S)	Percentage Error (%)	Maximum Bubble Radius (m)
#18 (590 g of C-4)	0.1345	0.2992	55.05	3.4545
#19(593 g of C-4)	0.1348	0.1426	5.47	3.4603

D. CONICAL SHAPED AND BLOCK EXPLOSIVE SOURCES COMPARISON

In this section, we are interested in the relationship between peak pressure and mass of C-4, and energy fluence. Underwater acoustic events are typically detected using peak pressure [16, 17]. Therefore, peak pressure is significant because it impacts our ability to detect those detonations. The energy fluence is be defined as

$$Ef = \int \frac{p^2(t)}{\rho c} dt, \tag{3.1}$$

where p is received acoustic pressure from the explosion, ρ is the bulk density of environment, in this case is the density of ocean, and c is the speed of sound.

The peak pressure and energy fluence of the acoustic signals are compared to the detonation weight in this section. The unit of $\mathbf{P_{max}}$ here is MPa. Then the energy fluence can also be obtained from the square values of pressures inside the range, and units of energy fluence is J/m^2. Energy fluence is sensitive to the integration time, and thus three values of 1, 0.5, and 0.05 s were used to calculate it. Table 7 lists these results and Figure 25 is a plot of energy fluence and peak pressure versus weight. We believe that more accurate energy fluence estimates are made using an integration time of 0.05 s due to the short durations of the pulse. Longer times may result in ambient or thermal noise being included in the energy fluence calculations.

Table 7. Conical Shaped Charge and Block Explosive Sources Comparison

Date (2019)	**Det #**	**Site. Depth [fsw]**	**C -4 [g]**	**Data-Sheet [g]**	**P_{max} [Pa]**	**E_f [$\frac{j}{m^2}$] (1s)**	**E_f [$\frac{j}{m^2}$] (0.5s)**	**E_f [$\frac{j}{m^2}$] (0.05s)**
15 APR	1	Land	201	36	N/A	N/A	N/A	N/A
	2		197	32	N/A	N/A	N/A	N/A
	3		213	31	N/A	N/A	N/A	N/A
16 APR	4	UW 30	214	29	5.12e+04	4.62e+04	4.40e+04	3.74e+04
17 APR	5		215	35	9.52e+04	1.26e+05	1.21e+05	1.19e+05
	6		209	34	2.43e+04	1.72e+04	1.60e+04	1.19e+04
	7(D)		215	29	5.27e+04	7.39e+04	7.20e+04	6.73e+04
	8(D)		196	33	6.51e+04	6.79e+04	6.56e+04	5.72e+04
18 APR	9(D)	UW 32	226	31	2.42e+04	3.52e+04	3.37e+04	2.73e+04
	10(D) (C-4 only)		567	0	4.68e+04	4.91e+04	4.70e+04	4.12e+04
	11 (C-4 only)		569	0	1.44e+05	5.67e+05	5.51e+05	5.42e+05
19 NOV	12	UW 45	176.0	15	6.82e+04	9.74e+04	9.35e+04	6.51e+04
	13		170.3	14	6.51e+04	9.63e+04	9.25e+04	8.21e+04
	14(D)		170.7	14	1.01e+05	2.67e+05	2.59e+05	2.51e+05
	15(D)		175.9	14	1.43e+05	2.80e+05	3.15e+05	3.02e+05
20 NOV	16	UW 45	170.2	16	6.20e+04	3.45e+04	3.28e+04	2.93e+04
	17		176.0	13	4.41e+04	4.92e+04	4.68e+04	3.04e+04
	18(D) (C-4 only)	UW 45	590	0	6.92e+04	2.44e+05	2.35e+05	2.06e+05
	19(D) (C-4 only)	UW 60-70	593	0	2.47e+04	4.02e+04	3.79e+04	2.31e+04
21 NOV	20	Land	176.5	14	N/A	N/A	N/A	N/A
	21		175.5	14	N/A	N/A	N/A	N/A
Prepared by: LT Chris Price, LT Wei-Ming (Andy) Chiu UW = Underwater; fsw = feet seawater; D = Double detonations with few seconds								

Figure 25 shows a scatter plot between C-4 weight and peak pressure (left-side), and energy fluence (right-side). The red asterisk denotes shaped charges, and the green asterisk denotes block charges. Surprisingly, there is no similarity or trend between values of peak pressure or energy fluence versus the weight of C-4 for the two types of explosive methods. There are several potential factors that could account this difference. First, there is some variability in where the detonations occurred, as the boat deploying

the explosive sources drifted during the experiment. Second, the location, which includes the range and depth of the detonations, will impact the same weight of explosives. Third, the explosions are not perfectly consistent, and some of the materiel in each shot may not have detonated, making the explosive yield different from the mass of explosive used.

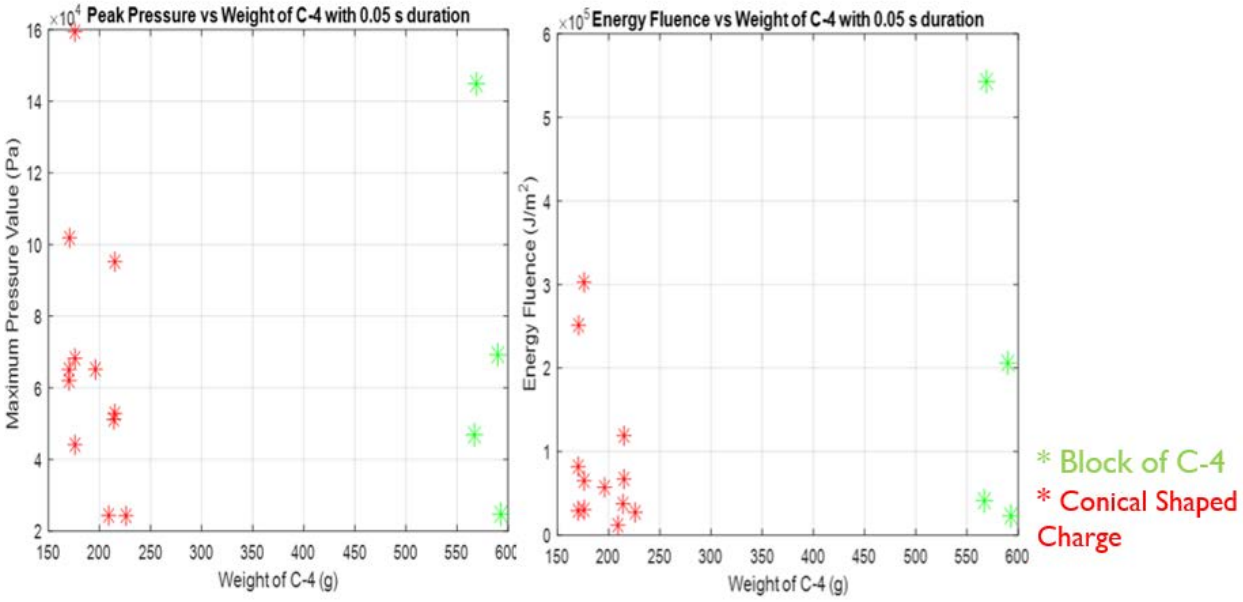
Peak Pressure vs Weight of C-4 with 0.05 s duration
Maximum Pressure Value (Pa)
Weight of C-4 (g)
Energy Fluence vs Weight of C-4 with 0.05 s duration
Energy Fluence (J/m²)
Weight of C-4 (g)
* Block of C-4
* Conical Shaped Charge

Red = detonations from Conical Shaped Charge; green = detonations from block of C-4.

Figure 25. Peak Pressure (Left) and Energy Fluence (Right) vs C-4 Weight

E. ASSESSING THE DISCREPANCIES USING ACOUSTIC SIMULATION

In this section, acoustic simulations were used to assess the discrepancy in peak pressure and energy fluence between detonations 18 and 19 from experiment 2. Because of the different source locations, both the range and the depth of the source are different between the two shots. This is demonstrated through modeling. Table 8 provides the input parameters of simulated detonations 18 and 19.

Figure 26 shows the temperature and salinity profile versus depth, and Figure 27 provides the density and sound speed profile versus depth, based on the CTD data during the second experiment. The second day had a greater sound speed due to increased

seawater temperature and higher PPS of the salinity. This sound speed profile was used to run the acoustic simulation according to this data.

Table 8. Input Parameter of Simulation

Simulation Detonations #	C-4 [g]	Receiver Depth [meter]	Site Depth [meter]	Distance from the receiver [m]
#18	746	≅15	≅15	≅800
#19	746	≅15	≅20	≅1050

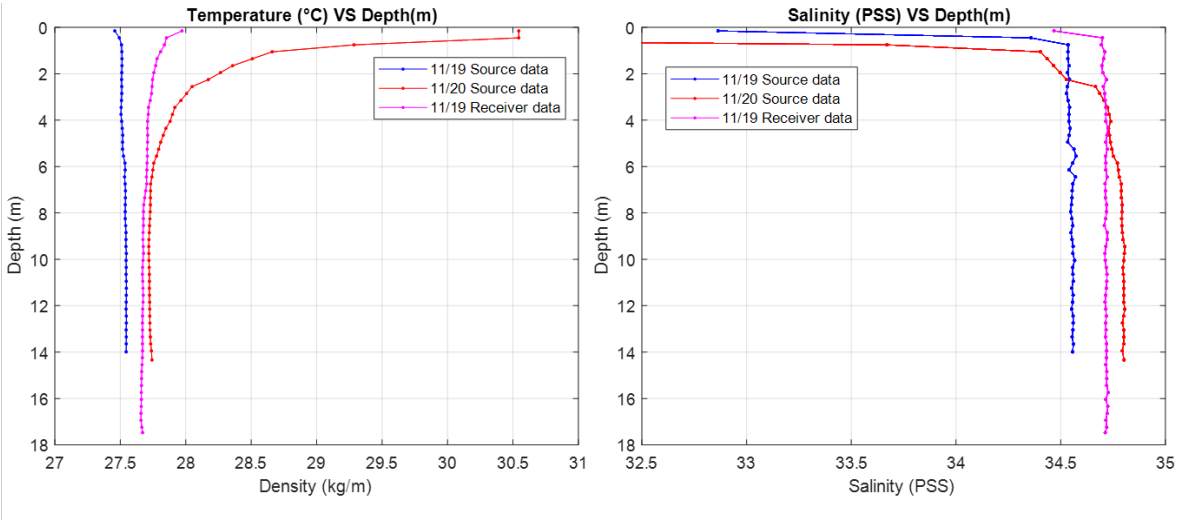

Figure 26. Temperature Profile (left); Salinity Profile (right)

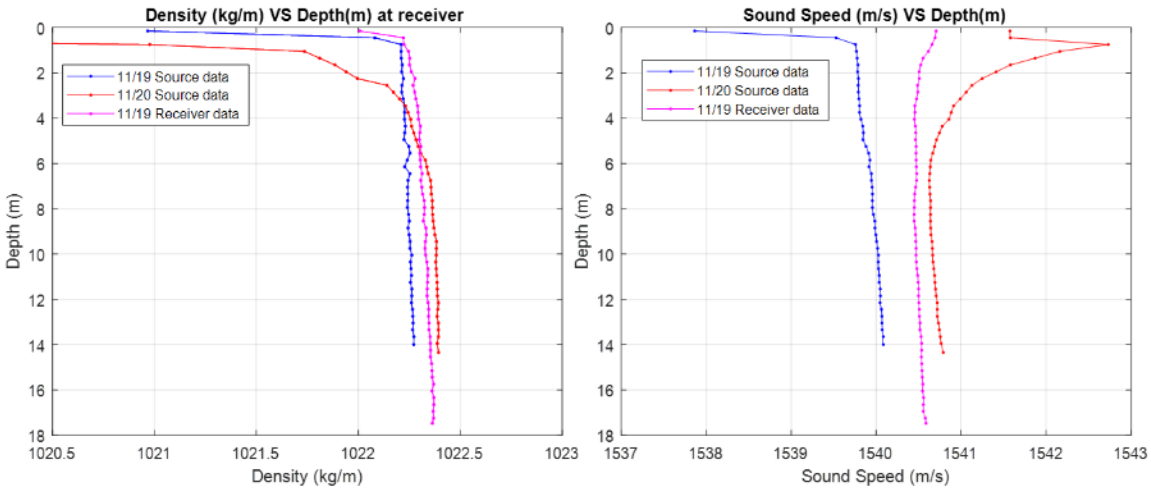

Figure 27. Density Profile vs. Depth (left); Sound Speed Profile vs. Depth (right)

The acoustic simulation was conducted with MATLAB and RAM using the PE model with range dependent bathymetry. A constant slope between source and receiver was assumed. The explosive source model is from Wakely [12], which predicts the time-domain response in the near field from an explosive source. Then, a parabolic equation model was used to calculate the transfer function of the environment. Fourier synthesis was used to compute the time-domain pressure. The environmental inputs were based on the data we obtained from CTD for the second experiment.

Figure 28 shows two simulated received signals in the time domain, one from the location of shot 18 with the 784 m range, and the other from the location of shot 19 with the 1056 m range. The peak pressures of the 784 m range signal (detonation 18) is greater than those for the 1056 m range signal (detonation 19). Also, after the primary peak, the secondary peak pressure shows up a few milliseconds later due to the bubble pulse. The secondary peak also shows reduced amplitude at longer ranges, which is expected. Overall, Figure 28 shows a difference of almost 6 dB between the two locations, which is equivalent to four times in the linear magnitude scale.

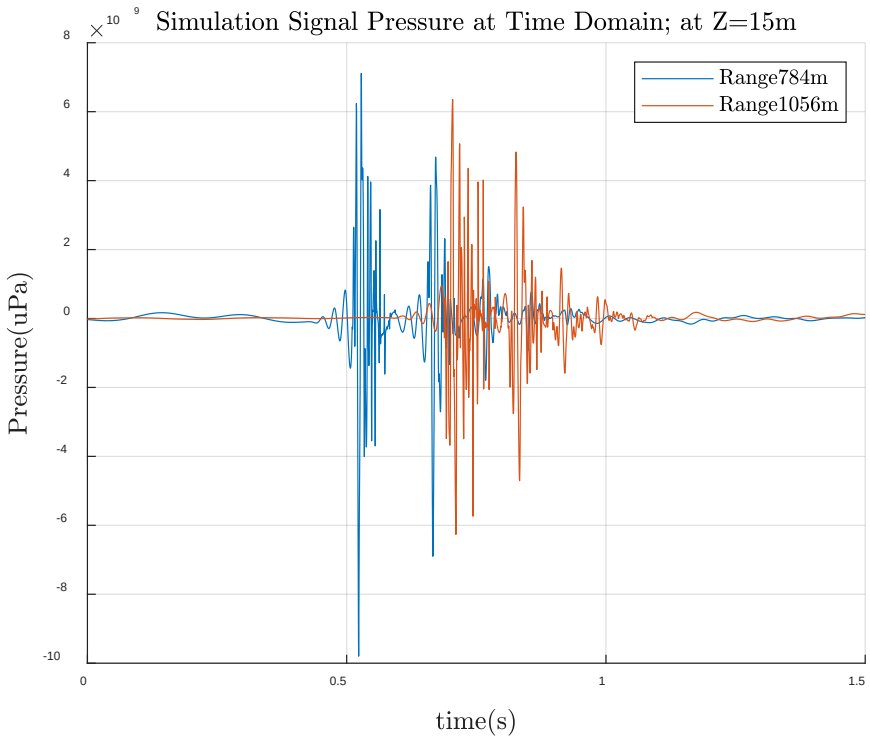

Figure 28. Two Simulated Signals with Two Difference Ranges

After we obtained the simulation results, we calculated the peak pressure and energy fluence. Table 9 shows the results from the simulation for the peak pressure and energy fluence, and Table 10 presents the empirical results for detonations 18 and 19, respectively. Both sets of results illustrate the detonation with shorter range has the stronger peak pressure and energy fluence, but the results for both peak pressure and energy fluence from the simulation were much smaller than the empirical results. A potential explanation for this discrepancy could be that computational limitations required a maximum frequency of 1600 Hz. Furthermore, in the experiment, there could have been a greater amount of high frequency content in shot 19 than in shot 18. Figure 29 shows the signal pressure in time domain. It shows the similar results of detonations 18 and 19. Figure 30 shows the power spectrum from simulated shots 18 and 19.

Table 9. Peak Pressure and Energy Fluence from Simulation for Detonations 18 and 19

Simulation Detonations #	C-4 [g]	Receiver Depth [m]	Site Depth [m]	Distance from the Receiver [m]	Peak Pressure [Pa]	Energy Fluence E_f [$\frac{j}{m^2}$] (0.05s Duration)
#18	590	≅15	≅15	≅800	7.5674e+03	7.9483e+03
#19	593	≅15	≅20	≅1050	6.1342e+03	5.9312e+03

Table 10. Peak Pressure and Energy Fluence from Experimental Data for Detonation 18 and 19

Experimental Data Detonations #	C-4 [g]	Receiver Depth [m]	Site Depth [m]	Distance from the Receiver [m]	Peak Pressure [Pa]	Energy Fluence E_f [$\frac{j}{m^2}$] (0.05s Duration)
#18	590	≅15	≅15	≅800	2.3562e+05	2.0609 +05
#19	593	≅15	≅20	≅1050	3.7939 +04	2.3129 +04

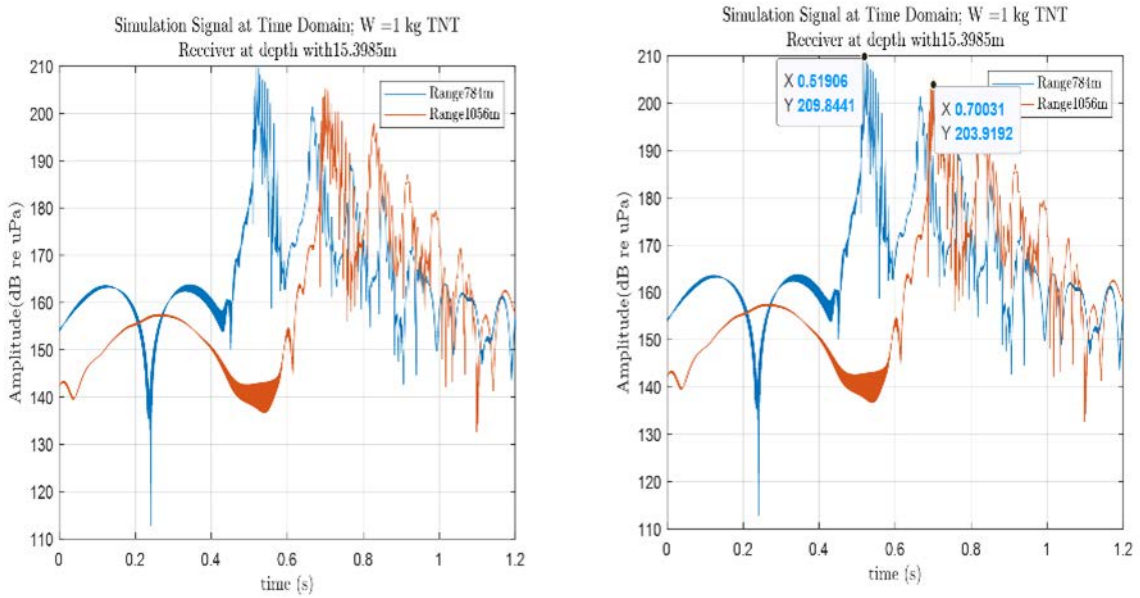

Figure 29. Simulated Signals Pressure at Receiver

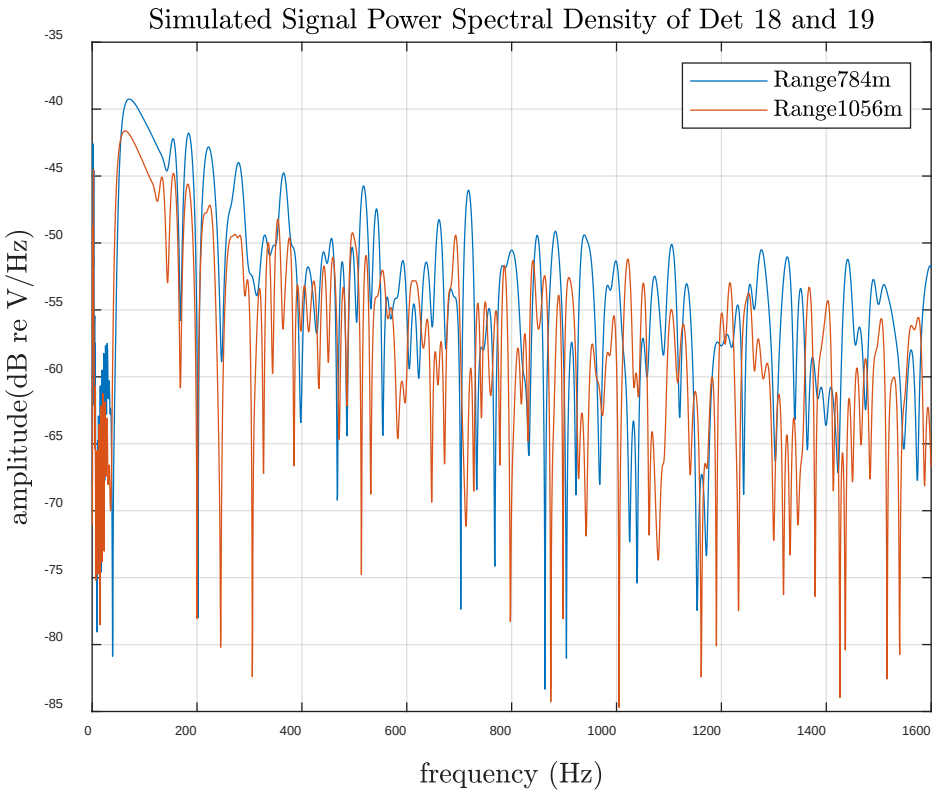

Figure 30. Simulated Signals of Detonations 18 and 19 at Frequency Domain

Figure 31 shows the spectrogram from the simulation where the distance between the source and receiver was 1,056 meters, and the source depth was 20 meters. A clear strong impulse can be identified after 0.746 s, and it persists for no longer than 200 ms. In this frequency domain plot, the modes interfered with each other and are not distinguishable from one another. Also, the relatively lower frequency ranges (0–800 Hz) have more energy than higher frequencies, which agrees with the experimental results.

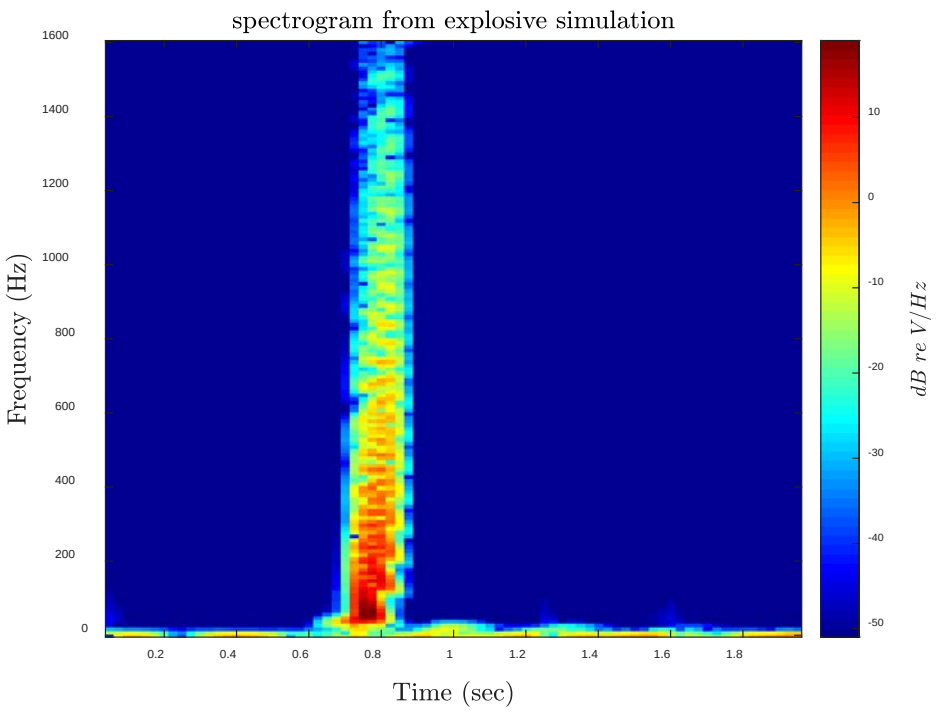

Figure 31. Spectrogram of Simulated Signal with 1,150 m Distance

Figure 32 shows how peak pressure changes as a function of depth and range. The difference between two peak pressures is 5.2 dB under the simulation's parameters. In this figure, we can see more generally how peak pressure changes with position. It decays with range, which is expected due to cylindrical spreading. It is also higher when the receiver is near the bottom due to the boundary conditions on the bottom and pressure released boundary conditions at the surface. Hence, the bottom, rather than the surface, will trap more sound in the waveguide.

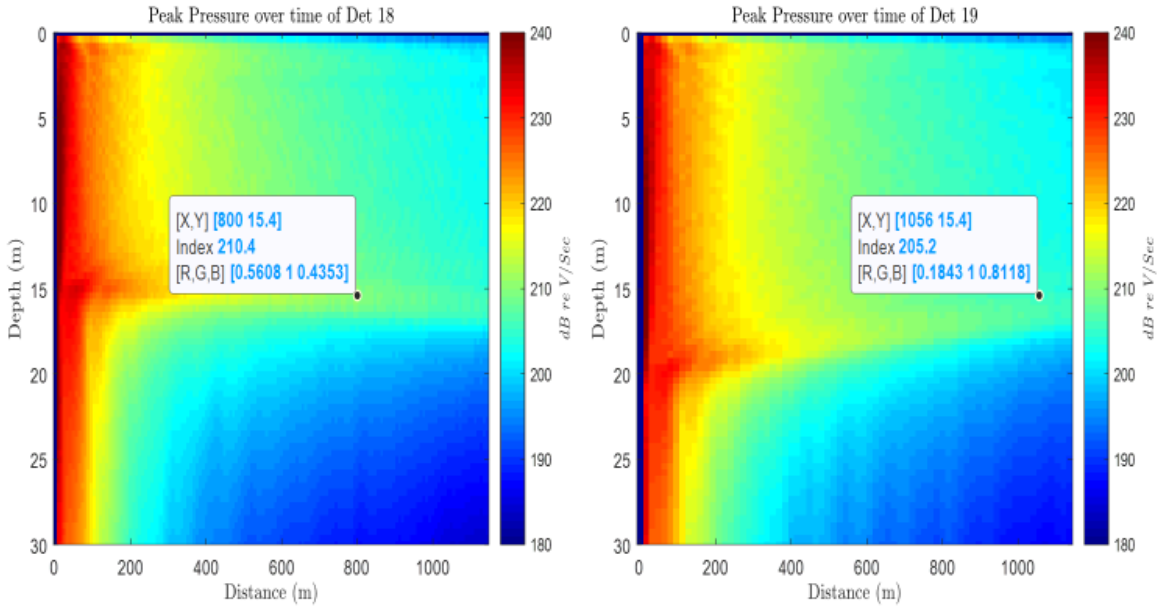

Figure 32. Peak Pressure Propagation from Two Cases of Simulation

In conclusion, the experimental results showed a large amount of variability in the peak pressure and energy fluence. In particular, two blocks of C-4 with similar mass had very different peak pressures and energy fluences. Due to wind and currents, these two detonations occurred at different locations, causing the source depth and range between the source and the receiver to differ. Simulations using the PE model (with much lower sampling frequency) indicated that these differences in peak pressure and energy fluence may be explained by the differing geometry.

THIS PAGE INTENTIONALLY LEFT BLANK

IV. SIMULATIONS IN OTHER ENVIRONMENTS

Given the differences in acoustic properties of explosions, noted in the previous chapter, we would like to understand the variability introduced by differences in the geography. Variations in depth, slope, and sediment composition may all have an impact on the peak pressure from explosive sources. In this chapter, five different key locations in the Indo-Pacific were chosen, according to their importance from the economic, commercial, and military perspectives, for simulations. The simulations followed the same procedures as were described in Chapter III.

A. SEDIMENT DATA AND BATHYMETRY

1. Sediment Physical Properties

Physical properties can be further refined into variables such as porosity, permeability, pore fluid, pore space characteristics, grain size, and sediment types. These properties have an effect on the sound speed and density of the seafloor. The grain size φ has been traditionally defined as $\varphi = -\log_2 d$ [18], where d represents the particle size in millimeters.

Another common way to classify sediment is based on the relative composition percentages (by weight) of sand, mud, silt, and clay that are present in a ternary phase diagram [19]. Figure 33 provides two examples based on sand-silt-clay ratios and sand-mud-gravel ratios of particles, respectively, in the three sides of the ternary diagram.

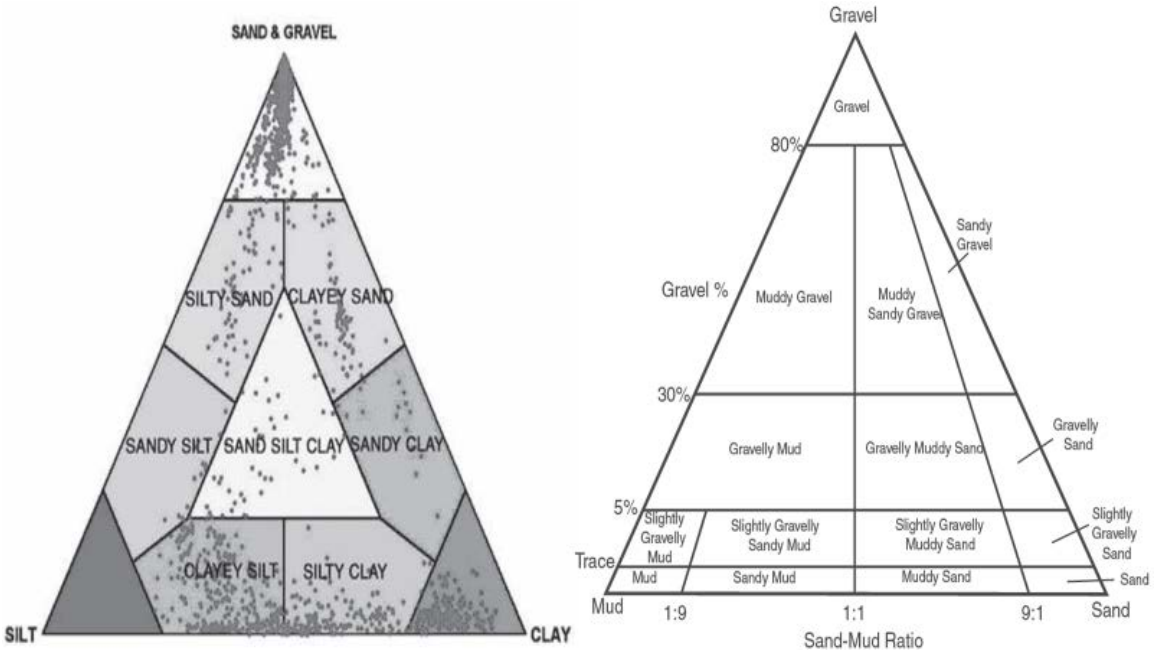

Left, source: [20]; right, source: [21].

Figure 33. Left: Ternary Diagram, Based on Sand-Silt-Clay Ratios; Right: Based on Gravel-Sand-Mud Ratios

2. Geoacoustic Properties

The geoacoustic properties play a pivotal part of sound propagation in the ocean. This includes speed and attenuation of compressional and shear waves, bulk density, and acoustic impedance. Speed impedance is also dependent on the temperature, salinity, and hydraulic pressure from the water depth [19]. General trends in geoacoustic properties for different types of sediments are given in Table 11.

Table 11. Geoacoustic Properties of Continental Shelf and Slope Environments.

Bottom	P (%)	ρ (kg/m^3)	C (m/s)	B (m/s)	α_p (dB/λ)	α_s(dB/λ)
Clay	70	1500	1500	<100	0.2	1.0
Silt	55	1700	1575	80z	1.0	1.5
Sand	45	1900	1650	110z	0.8	2.5
Gravel	35	2000	1800	180z	0.6	1.5
Moraine	25	2100	1950	600	0.4	1.0
Chalk	0	2200	2400	1000	0.2	0.5
Limestone	0	2400	3000	1500	0.1	0.2
Basalt	0	2700	5250	2500	0.1	0.2
Clay-Mud	N/A	1312	1470	<100	0.09	N/A

Adapted from [3] and Professor Colosi's class notes from Tactical Oceanography, OC4270, 4 February 2020.

3. Sediment Information Source

Sediment types are obtained from the *Database Description for Bottom Sediment Type (U)* version 2.0 from the Naval Oceanographic Office acoustic division. The database provides the acoustic simulation with inputs.

4. Justification for Study Sites

Figure 34 shows a map overview of the five areas of the Indo-Pacific region studied in this chapter. In terms of population, this region alone accounts for more than half of the population on this planet [22, 23]. Accordingly, economic and trade activity here amounts to more than half of all such activity globally [24]. In this region, sea lines of communication (SLOC) [25] are significant in supporting the large population and serve as the primary routes between major ports used for trading, logistics, and naval force purposes. Historically, the SLOCs have been important since WWII when the Japanese navy conquered most of the countries around this region. More recently, the importance of SLOCs has dramatically increased, especially since the People's Republic of China (PRC) opened up its economic market to the rest of the world. In October 2013, Chinese President Xi Jinping proposed the massive *One Belt One Road Initiative*, also known as the *Belt and Road Initiative* (OBOR or BRI), which is part of the Great China Dream [26]. The belt refers to the routes for road and rail transportation, known for

centuries as the silk road economic belt. In this case, “road” refers to the routes for sea trade, which is also known as the 21st Century Maritime Silk Road (MSR) [27]. Those areas studied here are straits along the same route as the MSR.

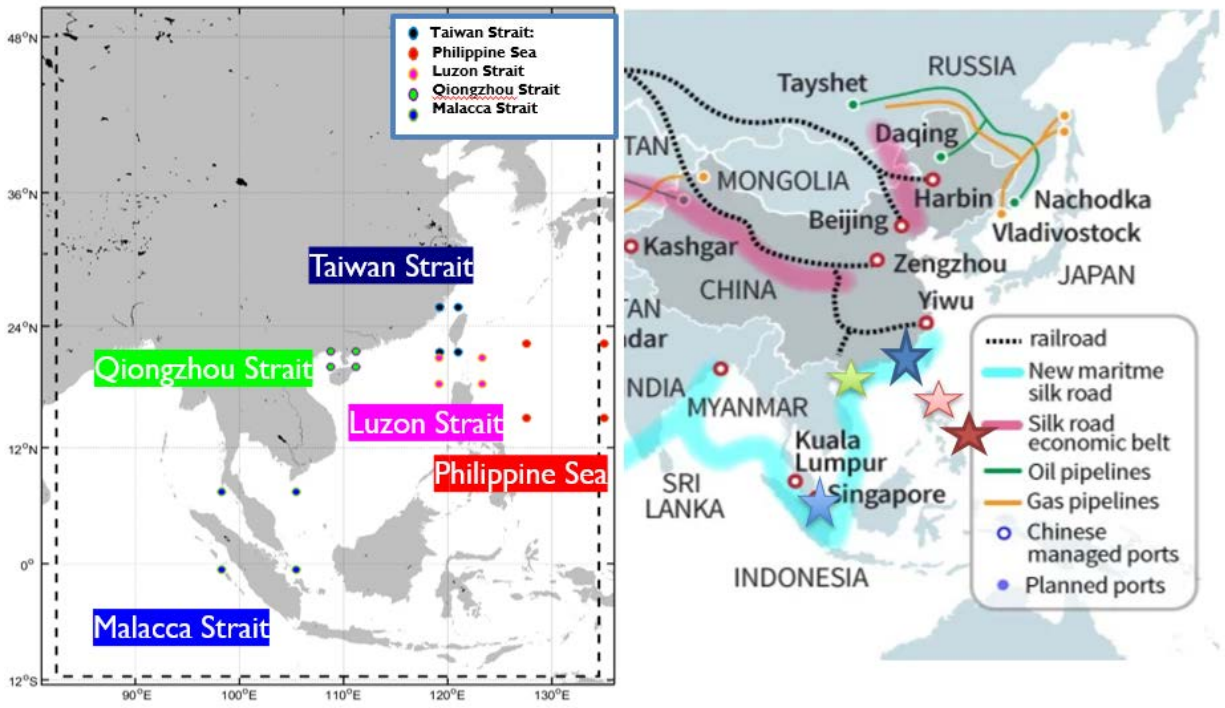

Adapted from [28] (right).

Figure 34. Map of Simulated Locations

5. Taiwan Strait

The Taiwan Strait is bounded by Mainland China to the west and Taiwan to the east. The Taiwan Strait is a relatively shallow strait, with an average water depth of 60 m [29]; it is 180 km wide and 350 km long. The strait factors prominently as a buffer between Taiwan and Mainland China, which have experienced a tense relationship since military confrontations in 1949. Diplomatic tension between the ROC (Taiwan) and the PRC, however, remains, and theirs is perhaps the most dangerous of the East Asian relationships [30].

Figure 35 shows the various seabed bottom types and Figure 36 shows the bathymetry in the Taiwan Strait . There are more than 20 different types of sediment. The primary sediment of this region is sand, including several kinds of sand, and the secondary sediment is silt of various kinds. After we know the particular bottom type of the area to be studied, we can determine the boundary condition of the bottom to exploit according to the geoacoustic properties of the specific sediments. Table 11 provides the geoacoustics for this region. Since the database does not profile an accurate ratio, however, the bottom sound speed of this region for the acoustic simulations will be an average of the sound speed corresponding to bottom types around Taiwan Strait, and this method is applied for the following four locations. The geoacoustic input and averaged value of this region can be obtained from Table 12, at the end of this section.

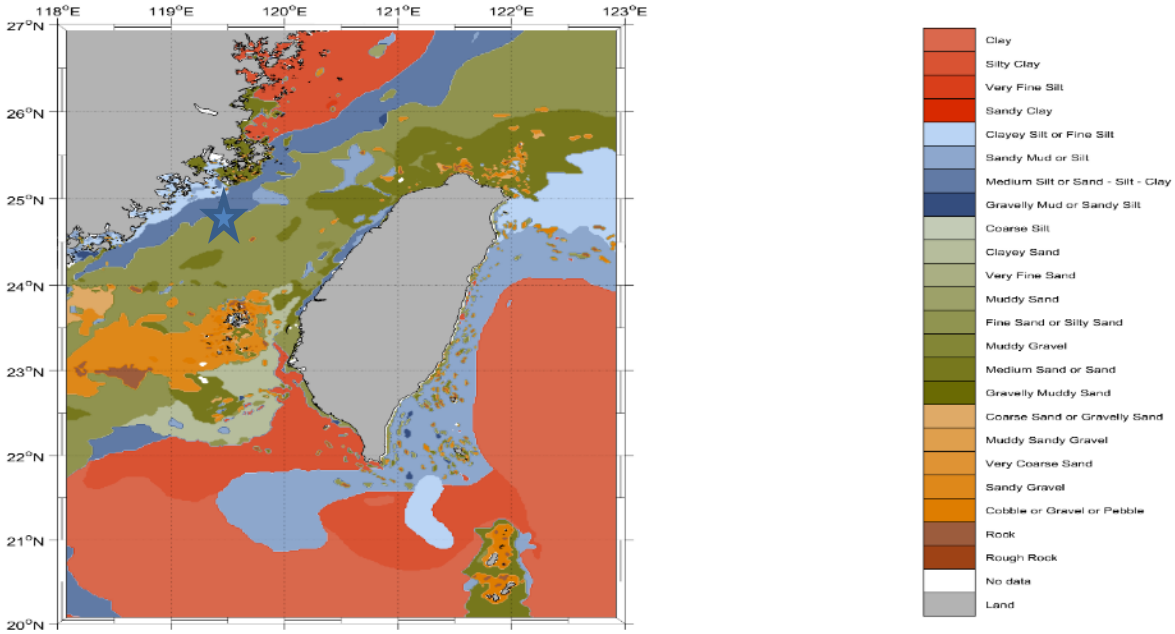

Figure 35. Taiwan Strait, Based on Bottom Type Database

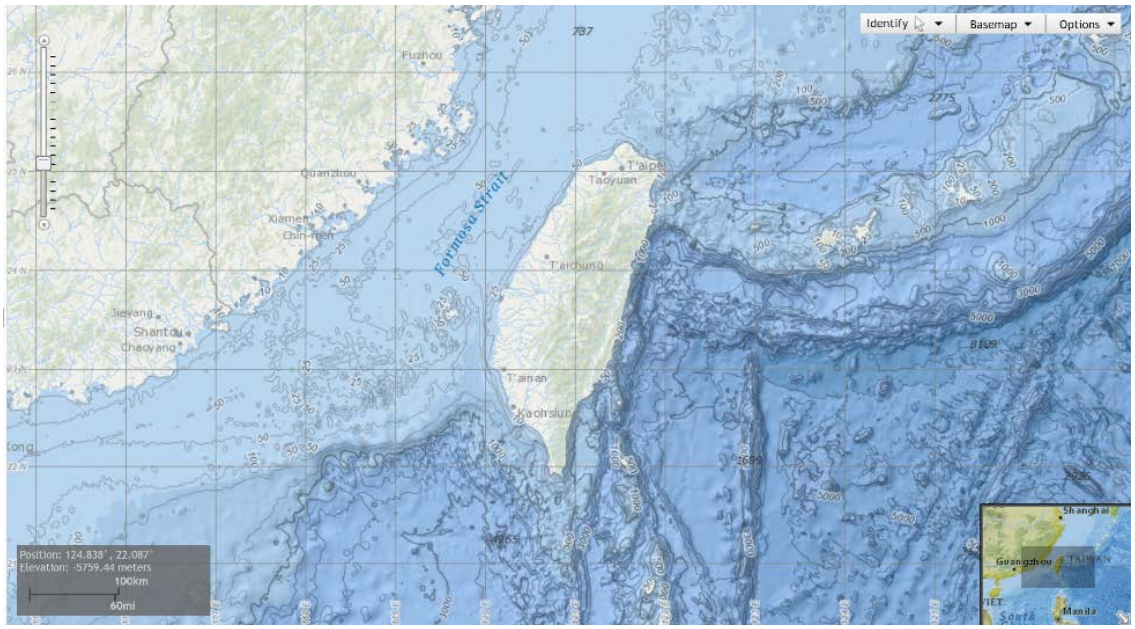

Figure 36. Taiwan Strait Bathymetry Data. Adapted from [31].

6. Philippine Sea

The Philippine Sea is bounded by the Philippines, Taiwan to the west, Japan to the north, the Marianas islands to the east, and Palau to the south. Moreover, it is a marginal sea with the Philippine Sea Plate coming from the floor of the sea that was originally formed from the western North Pacific Ocean [32, 33]. The Philippine Sea has traditionally been an old battlefield due to its location, through which ships must pass between the Southeast China Sea and East China Sea. Although the Philippine Sea is a relatively deep-water area, for the purposes of this thesis only a shallow water portion is studied.. This is due to the acoustic model used in this thesis, the PE method, which is very expensive to use for deep water environments. Based on the bottom type database, Figure 37 shows the few types of sediment and Figure 38 shows the bathymetry in this region. The primary sediment of this region is clay and the secondary sediment is silt of various kinds. Thus, the geoacoustic input and averaged value of this region based on the database can be obtained from Table 12.

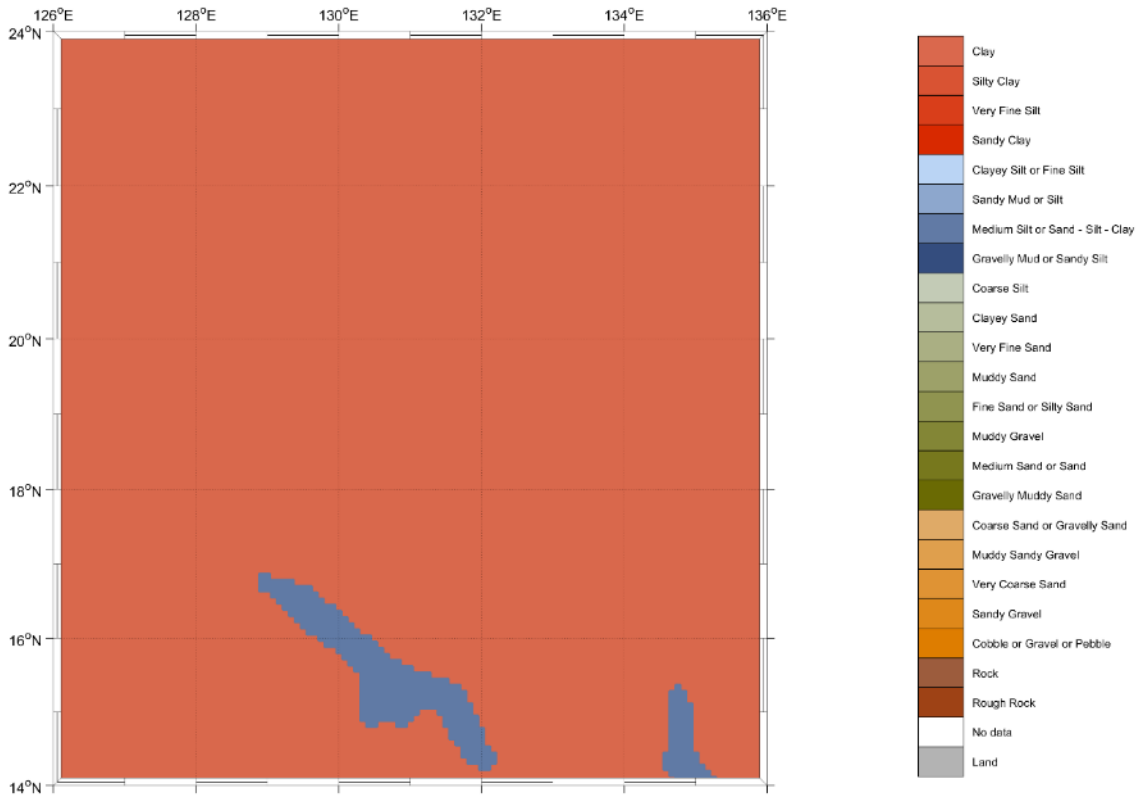

Figure 37. Philippine Sea, Based on Bottom Types Database

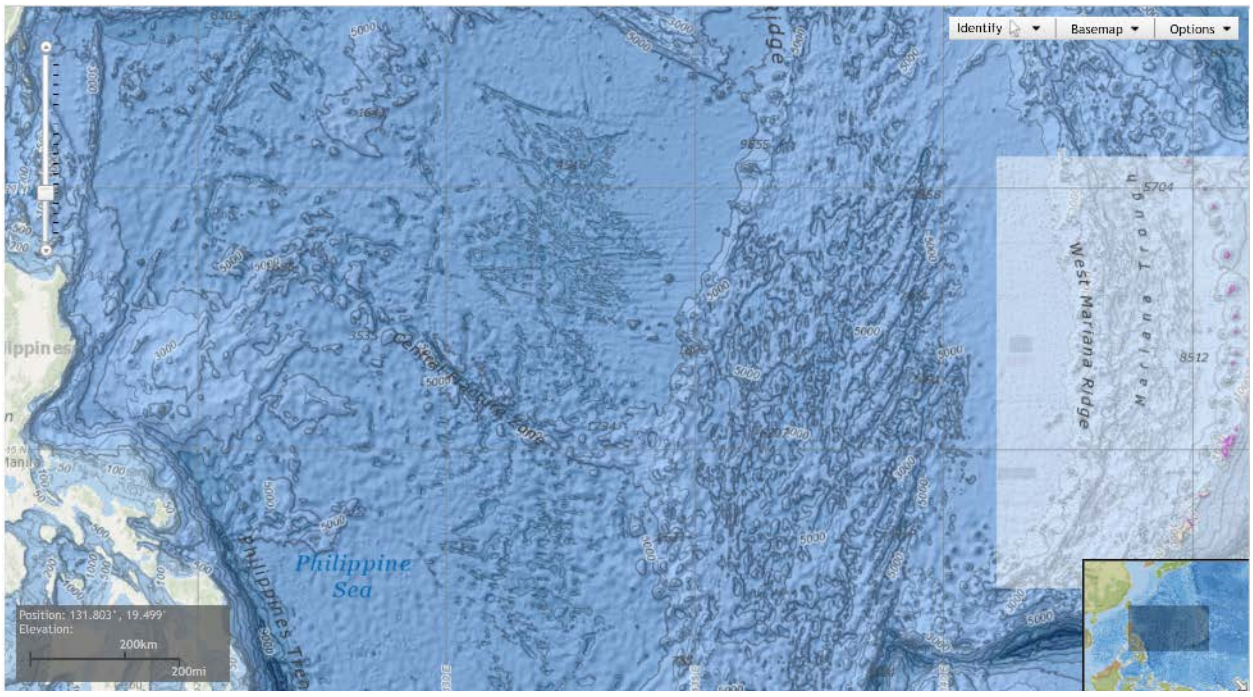

Figure 38. Philippine Sea Bathymetry Data. Adapted from [31].

7. Luzon Strait

The Luzon Strait is located between the Philippine island of Luzon and Taiwan. It is necessary to pass through the strait in sailing from the Philippine Sea to the South China Sea [33]. Like the Taiwan Strait, the Luzon Strait is another important strait for commerce and communication for the Philippines and surrounding countries [34]. The Luzon Strait is traversed by many undersea cables, which provide sharing of significant financial, informational, and military data among countries. The size of Luzon Strait is approximately 375 km length and 235–260 km wide [35]. Although the Luzon Strait is a relatively deep-water area in general, it includes many small islands and submerged rocks within the area. Moreover, it is the only deep water environment that connects the South China Sea and the Pacific Ocean. The deepest sill is around 2,400 m in the Bashi Channel [36]. The seafloor slope can be quite high in this region. Based on the simulation results, Figure 39 shows the several types and Figure 40 shows the bathymetry of sediment in this region. Figure 41 is the bottom topography of the South China Sea from another experiment [36]. The primary sediment of this region, though, is clay and the secondary sediment is gravel. So, based on information from the database, the geoacoustic input and averaged value of this region can be obtained from Table 12.

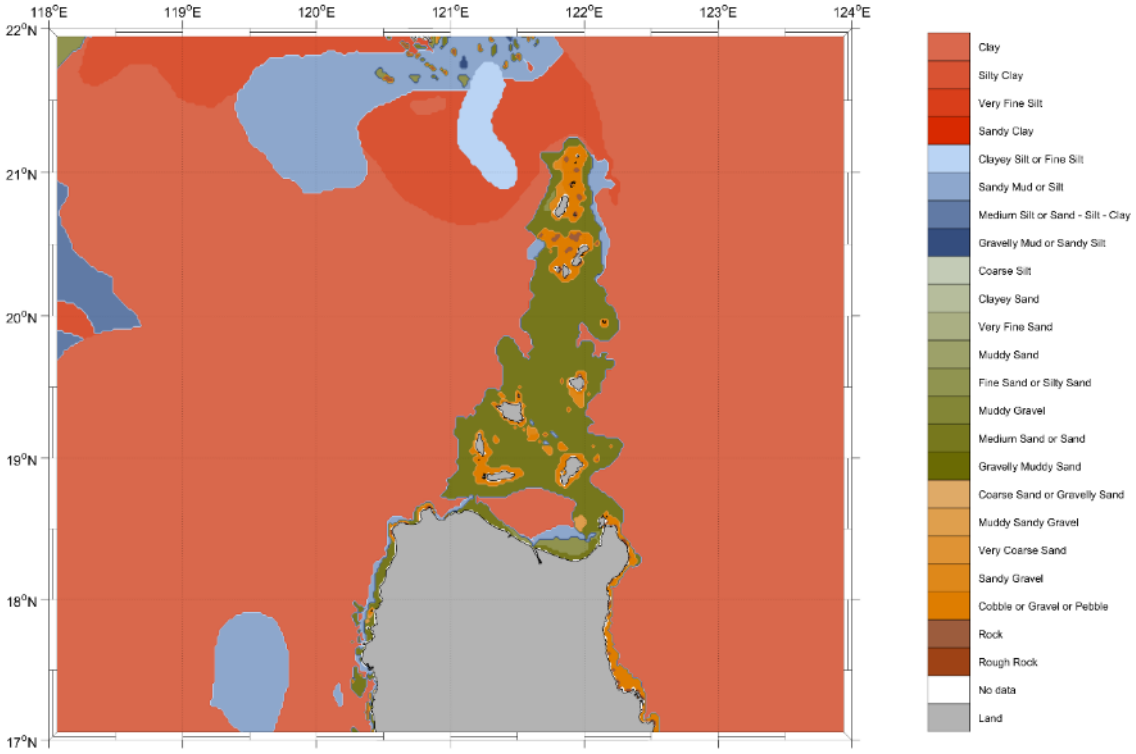

Figure 39. Luzon Strait, Based on Bottom Types Database

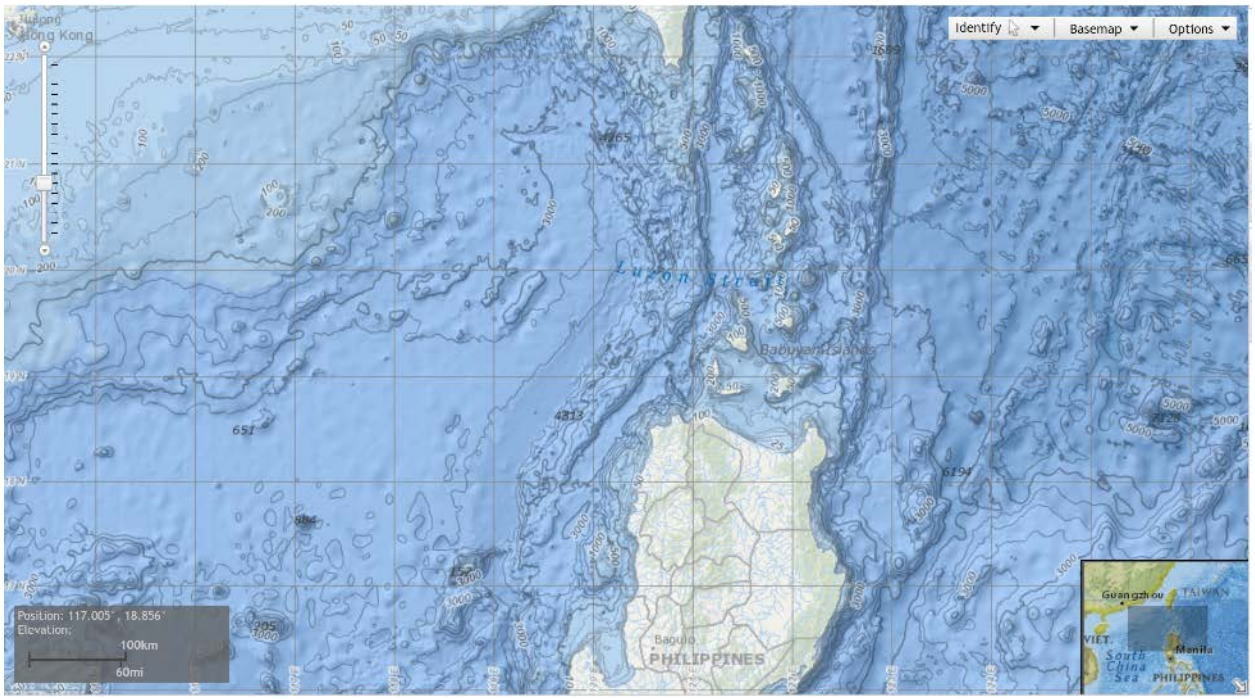

Figure 40. Luzon Strait Bathymetry Data. Adapted from [31].

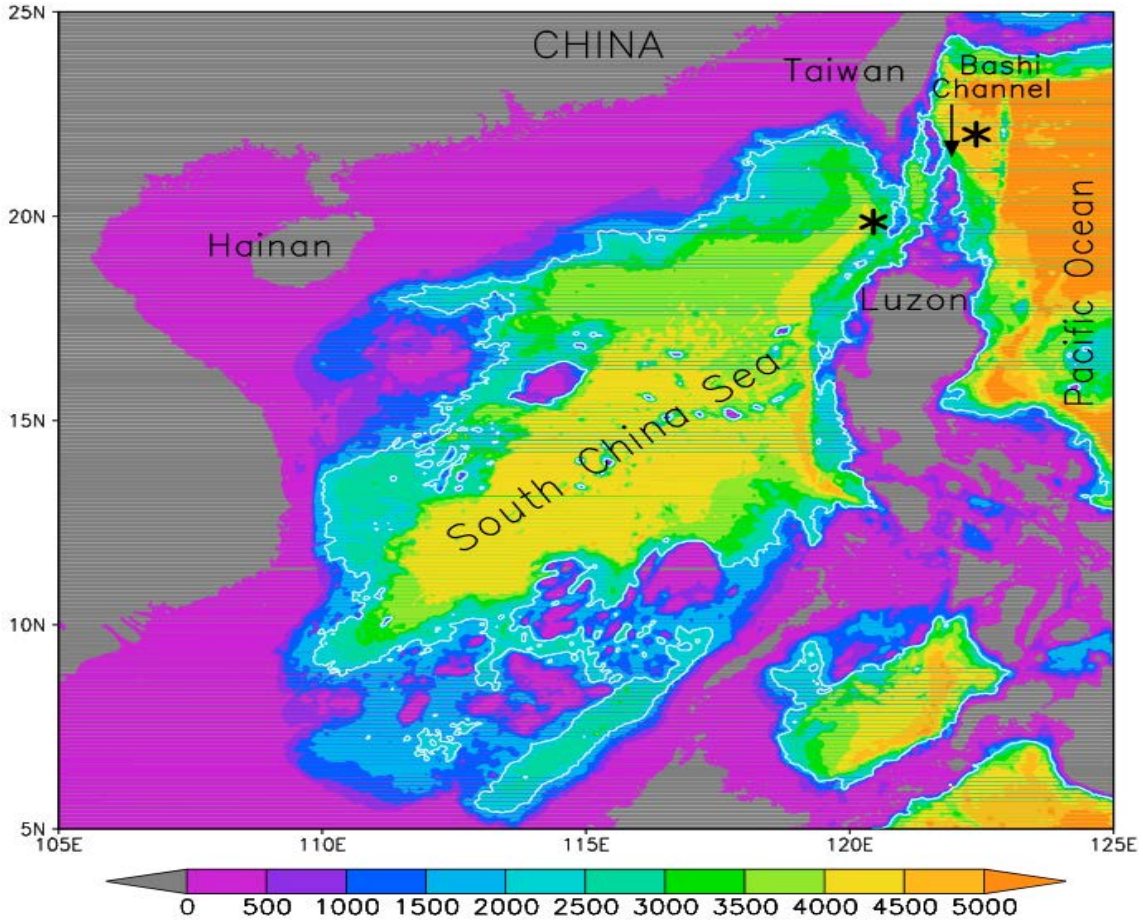

Figure 41. Bottom Topography of the South China Sea. Source: [36].

8. Qiongzhou Strait

The Qiongzhou Strait, also known as Hainan Strait, is located between Leizhou Peninsula in Guangdong province and Hainan Island (Hainan province). The Qiongzhou Strait is 30 km wide. Considered a relatively shallow water strait, its maximum depth is about 120 m [37]. Figure 42 shows the several types of sediment and Figure 43 shows the bathymetry in this region, based on the database. The primary sediment of this region is sand and the secondary sediment is silt. As with the previous location, the geoacoustic input and averaged value of this region, based on the database, can be inferred from Table 12.

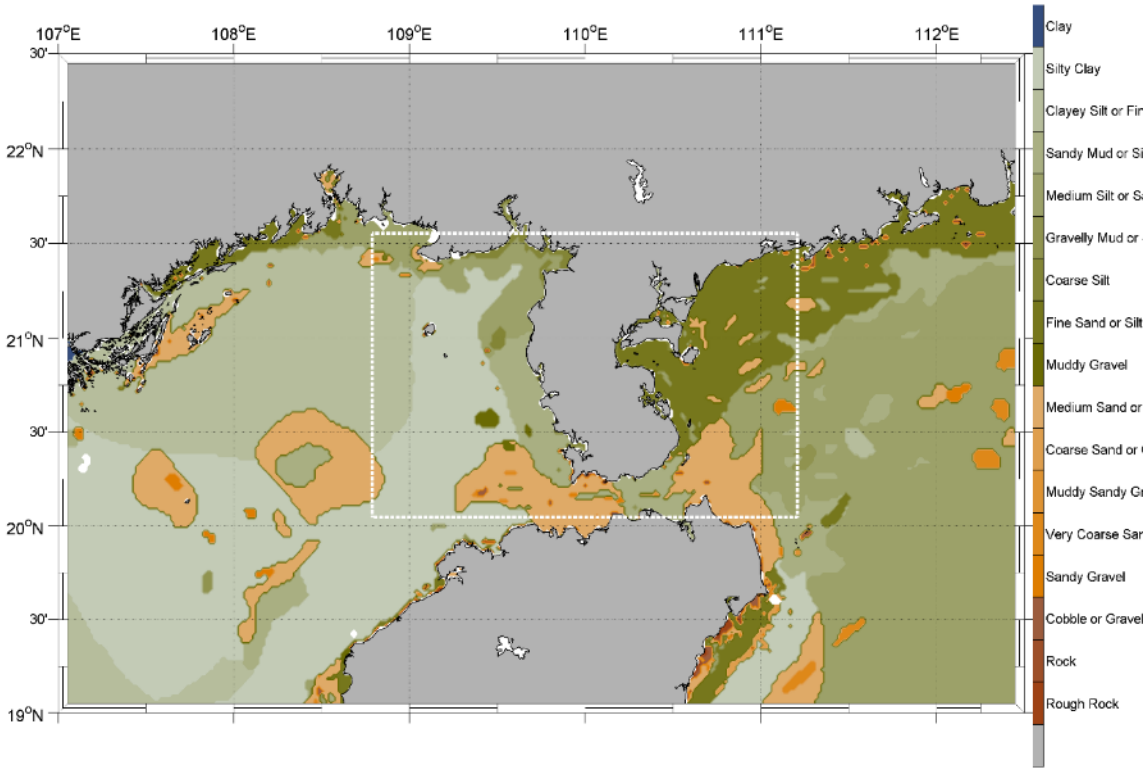

Figure 42. Qiongzhou Strait, Based on Bottom Type Database

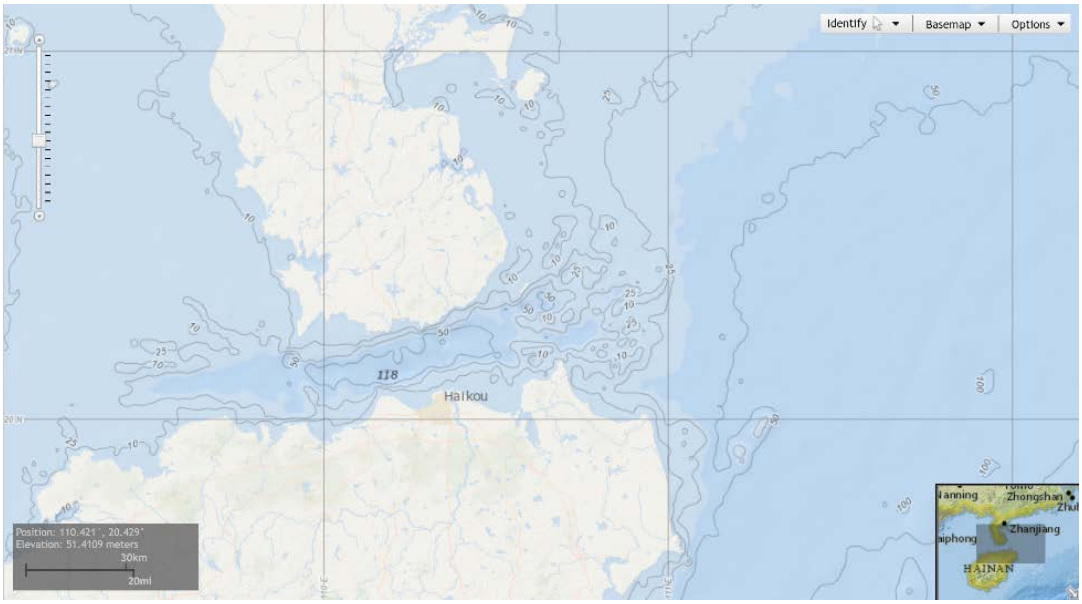

Figure 43. Qiongzhou Strait Bathymetry Data. Adapted from [28].

9. Malacca Strait

The Malacca Strait lies between the Malay peninsula of Malaysia and the island of Sumatra in Indonesia. As one of the busiest and most important shipping lanes in the world, this strait is the key waterway connecting the Indian Ocean and the Pacific Ocean. Furthermore, it is a shipping lane that links the major economies of the Indo-Pacific. Nearly 100,000 vessels pass through this strait annually. In 2016, more than 90 percent of the crude oil from the South China Sea passed through the Malacca Strait [38]. Although it is a shallow water passage, the Malacca Strait is approximately 805 km long and 64 km wide, with an average depth of 25 m [39].

Figure 44 shows the more than 20 types of sediment and Figure 45 shows the bathymetry in this region, based on the bottom type database. It illustrates the Malacca Strait region fully with various types of sediment. The primary sediment of this region is composed of several types of sand and the secondary sediment is silt of several kinds. Based on the results from the bottom type database, it is evident that the Malacca Strait and the Taiwan Strait share a strong similarity with respect to their many kinds of sediment and relatively shallow water regions in comparison with other regions. Furthermore, the geoacoustic input and averaged value of this region, based on the database, can be obtained from Table 12.

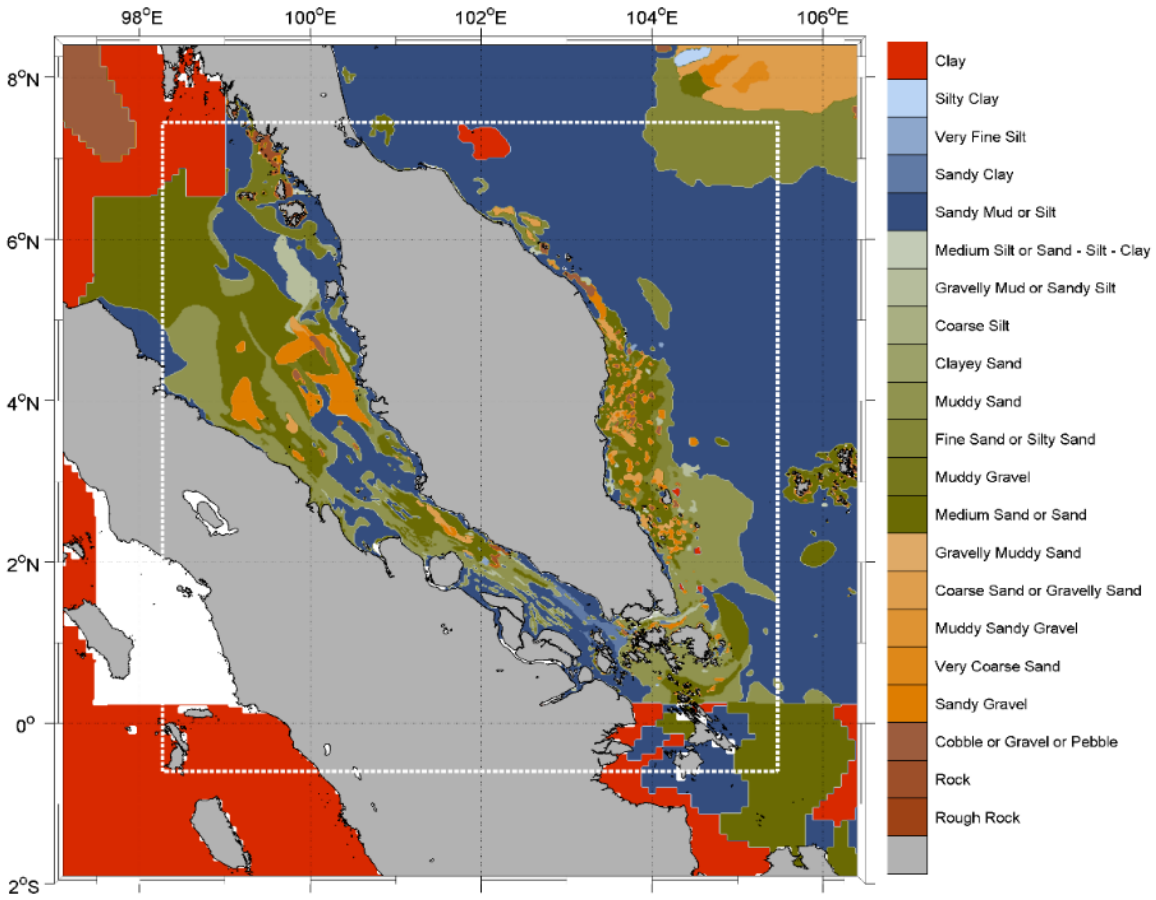

Figure 44. Malacca Strait, Based on Bottom Type Database

Figure 45. Malacca Strait Bathymetry Data. Adapted from [28].

Table 12. Input Parameters for Simulations of Five Locations.

Location	Latitude	Longitude	Depth [m] [min] [max]	Mean Grain Size of Components [mm]	Sound Speed [m/s]	Density [kg/m^3]	Attenuation [dB/λ]	Source Max Frequency [Hz]	Distance
Taiwan Strait	20°N 27°N	118°E 123°E	25 60	7.17 (Clayey silt) 2.53 (Fine sand) -6 (Gravel) 1.2333 (avg)	1575 (Silt) 1650 (Sand) 1800(Gravel) 1675 (avg)	1.745 (Clayey silt) 2.051 (Fine sand) -6 (Gravel) -0.7347 (avg)	1.5 (Silt) 2.5 (Sand) 1.5 (Gravel) 1.8333(avg)	1600 Hz	10km
Philippine Sea	14°N 24°N	126°E 136°E	50 500	10.94 (Clay); 7.17 (Clayey silt) 9.0550 (avg)	1500 (Clay) 1575 (Silt) 1537.5 (avg)	1.170 (Clay); 1.745 (Clayey silt) 1.4575 (avg)	1.0 (Clay) 1.5 (Silt) 1.25 (avg)	1600 Hz	10km
Luzon Strait	17°N 22°N	118°E 124°E	25 300	10.94 (Clay); -6 (Gravel) 2.4700 (avg)	1500 (Clay) 1800(Gravel) 1650 (avg)	1.170 (Clay); -6 (Gravel) -2.4150 (avg)	1.0 (Clay) 1.5 (Gravel) 1.25 (avg)	1600 Hz	10km
Qiongzhou	19°N 22.5°N	107°E 112°E	10 120	7.17 (Clayey silt) 2.53 (Fine Sand) 4.85 (avg)	1575 (Silt) 1650 (Sand) 1612.5 (avg)	1.745 (Clayey silt) 2.051 (Fine sand) 1.8980 (avg)	1.5 (Silt) 2.5 (Sand) 2 (avg)	1600 Hz	10km
Malacca Strait	2°S 8°N	98°E 106°E	10 50	10.94 (Clay); 7.17 (Clayey silt) 2.53 (Fine Sand) 6.88 (avg)	1500 (Clay) 1575 (Silt) 1650 (Sand) 1575 (avg)	1.170 (Clay); 1.745 (Clayey silt) 2.051 (Fine sand) 1.6377 (avg)	1.0 (Clay) 1.5 (Silt) 2.5 (Sand) 1.6667 (avg)	1600 Hz	10km

B. ACOUSTIC SIMULATION AND RESULTS ACROSS GEOGRAPHIC REGIONS

We obtained all geoacoustic properties from the database and as shown in Table 11. The values of the sound speed, density, and attenuation have been averaged due to a lack of accurate sediment ratios for each location. Rather than taking a portion of each sediment type, this study used the average data among primary sediments in that region. Furthermore, there is an important assumption this thesis made for acoustic simulation; namely, it assumes a half space simulation environment. This was chosen due to the absence of any detailed knowledge about the sub-surface layering. If that is known, for example, from a sub-bottom profiler, then this information could be incorporated into the mode. The simulations for the five regions are based on 500 kg of C-4 explosives and a range of 10 km. The Nyquist frequency of simulation was 800 Hz. All setting input parameters for the simulations were based on what was best suited for my computational capability and available time. All simulation input can be extended in range and frequency with additional computational resources. Figure 46 shows the results from the simulation for five significant locations in the Indo-Pacific region. The peak pressure map of each location varies according to its own bathometry and bottom boundary conditions. Figure 47 is the comprehensive result from acoustic simulation in this study. Note that the Qiongzhou Strait and Philippine Sea curves have the highest peak pressure as a function of range. This is likely due to the fact that both environments have down-slope propagation.

One of the purposes of this study is to explore how seafloor properties vary with location in order to see how the environment impacts the signal. To that end, Figure 47 shows not only how the peak pressure from the explosive source can be presented with an exponential decay but also the peak pressure variability across geographic regions. This can be used as an application when we want to look for the peak pressure for certain explosives at any location with basic bottom type information.

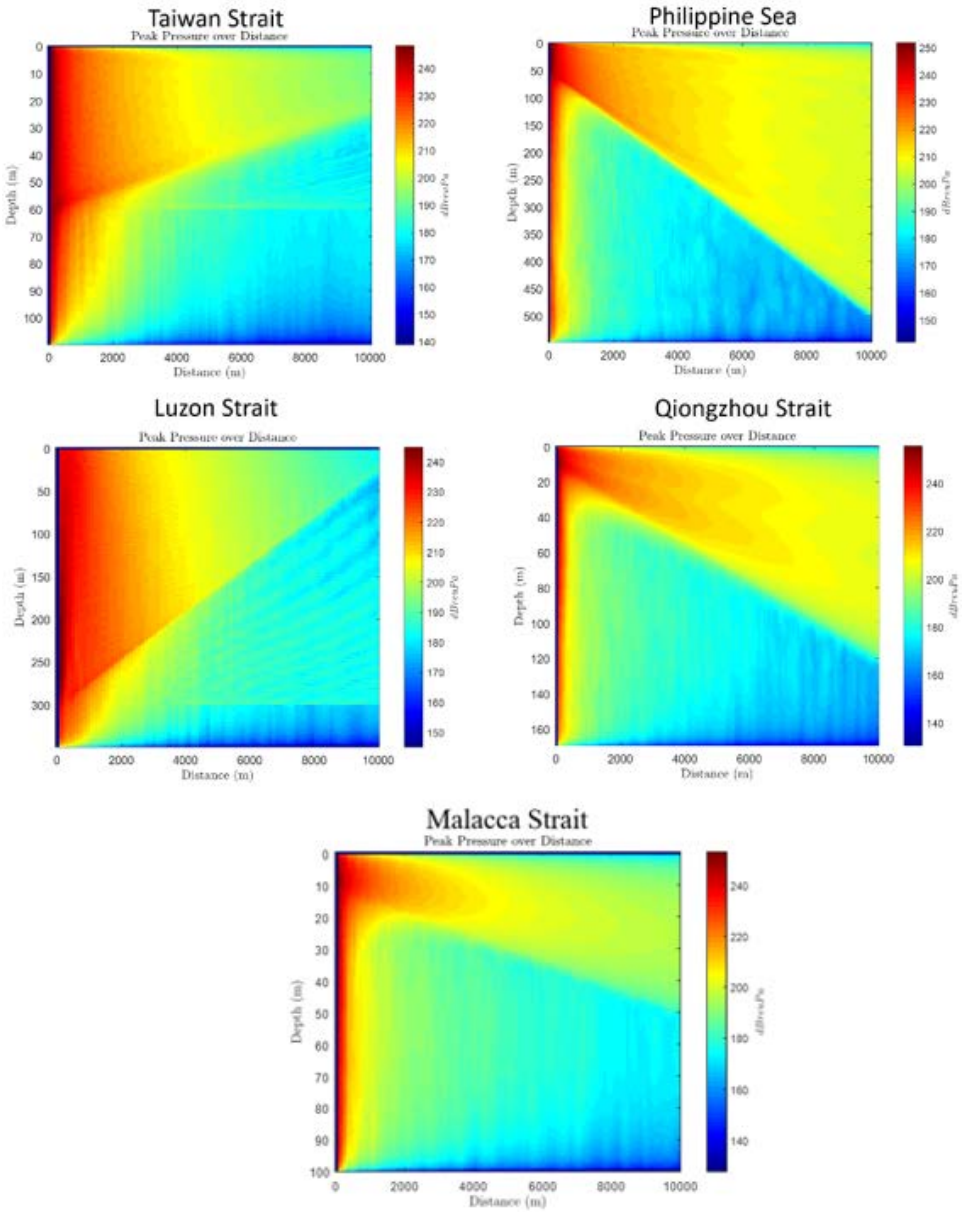

Figure 46. Simulated Peak Pressure Map of Five Locations

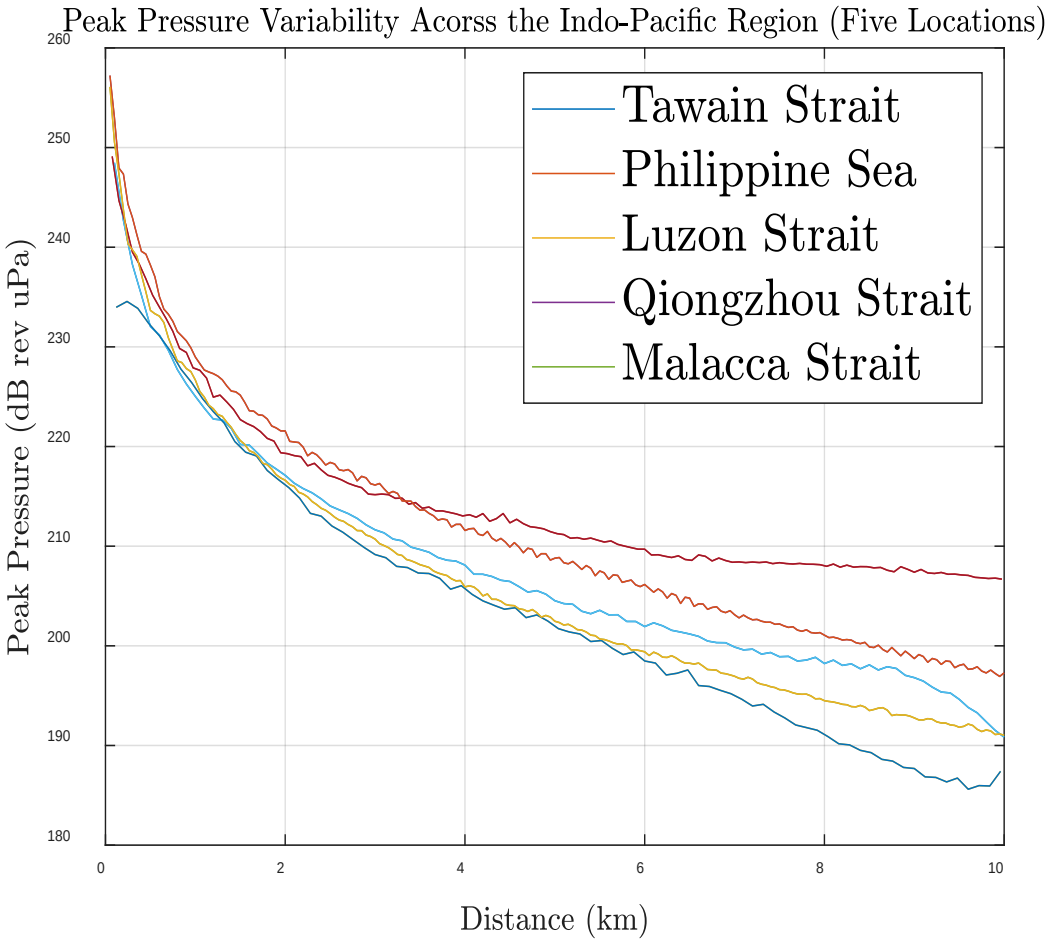

Figure 47. Peak Pressure Variability Across the Indo-Pacific Region

V. SUMMARY AND RECOMMENDATIONS FOR FUTURE WORK

A. SUMMARY

This study captures the basic framework of each UNDET during the spring and fall seasons for the shallow water nearshore location outside Pearl Harbor. These UNDETs also have been analyzed in relation to fluctuations in time, frequency domains, and by spectrogram. Furthermore, time delay methods and maximum bubble radius obtained from the received signal from the explosions were taken into consideration. As such, several useful figures were created from those five UNDET simulations, each corresponding to one of the five different locations. The figure representing the signal according to the time domain sheds light on the relationships between shock wave pressure and weight of explosive source. The figure representing the signal according to the frequency domain illustrates the amplitude's varying scale over the entire frequency for a broadband signal. Meanwhile, the spectrogram for simulated signal presents the main blast according to both the time and frequency domains. Furthermore, bubble numbers and mode dispersion can also be demonstrated with the spectrogram. The figure depicting peak pressure over time can illustrate the path of how waves propagate in an underwater environment. Findings from these simulations underscore the significance of depths and ranges on explosive wave propagation. Lastly, the figure depicting sound pressure level versus distance can help determine the maximum detection range. This range, for instance, could be calculated with a design receiving threshold in a dB scale. Similarly, this figure could also help the U.S. and Taiwan Explosive Ordnance Disposal personnel to have a better understanding of the distance they should maintain from UNDETs during operations.

B. RECOMMENDATIONS FOR FURTHER EXPLORATION

It is worth noting that this thesis was unable to find a trend between peak pressure or energy fluence and the weight of C-4 explosives due to various environmental and man-made factors. First, the measurements for the range between the receiver and the

source could be more accurate and consistent, which would require station monitoring from the boat from which the explosive sources were deployed. Concurrently, noise from the ship's propellers was one main type of ambient noise present in this study's experiment. Exploring ways to mitigate this factor would be valuable. Lastly, adjusting the range would be another notable improvement before conducting future field tests. As we found, the effect of the environment is reduced with shorter ranges, although longer ranges are more realistic for acoustic sensing networks. The relationship between sound pressure level and range of UNDETs, which was assessed in this study, contributes a solid foundation for future studies.

C. ENHANCED TECHNIQUES FOR FUTURE WORK

Several techniques offer potential for extracting information from the experimental measurements.

1. Time-warping

Time-warping is a simple and effective model exploiting normal mode propagation in shallow water environments, and can be used to isolate normal mode components [40] efficiently. The mode coefficients could be calculated after isolation, and the relative energy in each mode could be compared for different types of sources. In particular, this method would be able to determine whether conical shaped charges have acoustic directionality.

2. Acoustic Simulation with Directional Source

The standard simulated signal source for acoustic models is omni-directional. Although this study does not include directionality, it may be present in other types of explosive sources and bears examination. The parabolic equation model used here also assumes omnidirectional sources, but could be simulated by coherently summing several closely spaced point sources with linearly varying phases.

3. Closer Range Experiments

This research has collected data from the far range. In subsequent studies, it would be interesting to compare the signal received from explosions with shorter ranges. The signal should provide more precise information directly from explosion with less multi-paths interference during the propagation.

THIS PAGE INTENTIONALLY LEFT BLANK

VI. CONCLUSION

This thesis was focused on both experimental and simulated studies on explosive sources in shallow water within five locations in the Indo-Pacific region. The experimental results from explosive sources with a conical shaped charge and explosive source with a block C-4 show a large degree of variability but no consistent trend.

Furthermore, acoustic pressure, amplitude, spectrogram, and power spectral density from the explosive source were generated by acoustic simulation (RAM), which could give us more insight into how explosive waves are received in different environments. Specifically, this study demonstrates the simulations used to asses variability in peak pressure for the selected locations in the Indo-Pacific region.

Finally, the results of this research enhance the understanding of acoustic propagation of explosive sources in complex environments, which will be helpful to the navies of the United States and Taiwan in mine warfare. These results could be used to understand and enhance the requirements of an offensive mission requiring explosives in cross domain operations. Meanwhile, the developed simulation could be applied defensively to determine the optimal placement and number of sensors required to monitor undersea infrastructure.

THIS PAGE INTENTIONALLY LEFT BLANK

LIST OF REFERENCES

[1] R. Carlson, N. Christensen, and R. Wilkens, "Acoustic properties of volcaniclastic sediments recovered from the floor of the Philippine Sea, deep sea drilling project leg 59," Jan. 1, 1981. Available: https://doi.org/10.2973/dsdp.proc.59.111.1981.

[2] T.-H. Won and S.-J. Park, "Design and implementation of an omni-directional underwater acoustic micro-modem based on a low-power micro-controller unit," *Sensors,* vol. 12, no. 2, pp. 2309–2323, 2012.

[3] F. B. Jensen, W. A. Kuperman, M. B. Porter, and H. Schmidt, *Computational ocean acoustics*. New York, NY, USA: Springer Science & Business Media, 2011.

[4] F. D. Tappert, "The parabolic approximation method," in *Wave propagation and underwater acoustics*: New York, NY, USA: Springer, 1977, pp. 224–287.

[5] A. Radder, "On the parabolic equation method for water-wave propagation," *Journal of Fluid Mechanics,* vol. 95, no. 1, pp. 159–176, 1979.

[6] Leontovich and V. Fock, "Solution of the problem of propagation of electromagnetic waves along the earth's surface by the method of parabolic equation," *J. Phys. Ussr,* vol. 10, no. 1, pp. 13–23, 1946.

[7] P. Roux, H. Song, M. Porter, and W. Kuperman, "Application of the parabolic equation method to medical ultrasonics," *Wave Motion,* vol. 31, no. 2, pp. 181–196, 2000.

[8] A. Song, J. Senne, M. Badiey, and K. B. Smith, "Underwater acoustic communication channel simulation using parabolic equation," in *Proceedings of the Sixth ACM International Workshop on Underwater Networks,* 2011, pp. 1–5.

[9] S. De Candia, R. Ojeda, W. Reid, and M. Ratcliffe, "The whipping response of a submerged platform subjected to near-field, non-contact underwater explosions," Australia: Commonwealth of Australia, 2018. [Online]. Available: https://www.dst.defence.gov.au/sites/default/files/publications/documents/DST-Group-RR-0451.pdf

[10] F. A. Costanzo, "Underwater explosion phenomena and shock physics," in *Structural Dynamics, Volume 3*: New York, NY, USA: Springer, 2011, pp. 917–938.

[11] J. Hooper, "Weapons Physics," Naval Postgraduate School, unpublished, 2018.

[12] J. W. Jr., “Coherent ray tracing—measured and predicted shallow-water frequency spectrum,” *The Journal of the Acoustical Society of America,* vol. 63, no. 6, pp. 1820–1823, 1978, https://doi.org/10.1121/1.381920

[13] Wildlife Acoustics. “Song meter SM3M submersible and deep water bioacoustics recorder.” Accessed Feb. 01, 2020. [Online]. Available: https://www.wildlifeacoustics.com/images/documentation/SM3M-USER-GUIDE.pdf

[14] Wildlife Acoustics. “Song Meter SM3M submersible and deep water.” Accessed Nov. 20, 2019. [Online]. Available: https://www.wildlifeacoustics.com/uploads/user-guides/SM3M-USER-GUIDE.pdf (accessed Nov 20, 2019).

[15] Acousonde. “Acousonde 3A.” [Online]. Available: http://www.acousonde.com/downloads/Acousonde3A_Brochure.pdf

[16] W. W. Au and K. J. Snyder, “Long-range target detection in open waters by an echolocating Atlantic Bottlenose dolphin (Tursiopstruncatus),” *The Journal of the Acoustical Society of America,* vol. 68, no. 4, pp. 1077–1084, 1980.

[17] D. Kapolka, “Underwater acoustics for naval applications,” Naval Postgraduate School, unpublished, 2012.

[18] W. C. Krumbein, “Size frequency distributions of sediments,” *Journal of sedimentary Research,* vol. 4, no. 2, pp. 65–77, 1934.

[19] D. R. Jackson, M. D. Richardson, *High-Frequency Seafloor Acoustics*. Springer, New York, NY, USA. 2007.

[20] F. P. Shepard, “Nomenclature based on sand-silt-clay ratios,” *Journal of Sedimentary Research,* vol. 24, no. 3, pp. 151–158, 1954.

[21] R. L. Folk, *Petrology of Sedimentary Rocks*. Hemphill Publishing Company, 1980.

[22] C. Hackett. “Which 7 countries hold half the world’s population?” Accessed Feb 3, 2020. [Online]. Available: jttps://www.pewresearch.org/fact-tank/2018/07/11/world-population-day/

[23] PACOM. “USPACOM Area of Responsibility.” Accessed March 1, 2020. [Online]. Available: https://www.pacom.mil/About-USINDOPACOM/USPACOM-Area-of-Responsibility/

[24] Economic Times. “Navigating the Indo-Pacific cooperation.” [Online]. Available: https://economictimes.indiatimes.com/blogs/et-commentary/navigating-the-indo-pacific-cooperation/

[25] R. B. Peele, “Maritime Chokepoints: Key Sea Lines of Communication (SLOCs) and Strategy,” Army War College, Carlisle Barracks PA, 1997.

[26] P. Ferdinand, “Westward ho—the China dream and ‘one belt, one road’: Chinese foreign policy under Xi Jinping,” *International Affairs*, vol. 92, no. 4, pp. 941–957, 2016.

[27] C. Len, “China’s 21st Century Maritime Silk Road initiative, energy security and SLOC access,” *Maritime Affairs: Journal of the National Maritime Foundation of India*, vol. 11, no. 1, pp. 1–18, 2015.

[28] CTW. “The Belt and Road—The China Trade Week—KSA 2020.” Accessed Feb. 18, 2020. [Online]. Available: http://www.ctwsaudi.com/page/market.aspx

[29] S. Jan, J. Wang, C.-S. Chern, and S.-Y. Chao, “Seasonal variation of the circulation in the Taiwan Strait,” *Journal of Marine Systems*, vol. 35, no. 3–4, pp. 249–268, 2002.

[30] D. Roy, “Tensions in the Taiwan Strait,” *Survival*, vol. 42, no. 1, pp. 76–96, 2000.

[31] NOAA. “Bathymetric Data Viewer.” Accessed Feb. 17, 2020. [Online]. Available: https://maps.ngdc.noaa.gov/viewers/bathymetry/

[32] T. Seno and S. Maruyama, “Paleogeographic reconstruction and origin of the Philippine Sea,” *Tectonophysics*, vol. 102, no. 1–4, pp. 53–84, 1984.

[33] P. F. Worcester et al., “The North Pacific Acoustic Laboratory deep-water acoustic propagation experiments in the Philippine Sea,” *The Journal of the Acoustical Society of America*, vol. 134, no. 4, pp. 3359–3375, 2013.

[34] J. Locat and J. Mienert, *Submarine Mass Movements And Their Consequences: 1st International Symposium*. New York, NY, USA: Springer Science & Business Media, 2012.

[35] D.-L. Tang, I.-H. Ni, D. R. Kester, and F. E. Müller-Karger, “Remote sensing observations of winter phytoplankton blooms southwest of the Luzon Strait in the South China Sea,” *Marine Ecology Progress Series*, vol. 191, pp. 43–51, 1999.

[36] T. Qu, J. B. Girton, and J. A. Whitehead, “Deepwater overflow through Luzon Strait,” *Journal of Geophysical Research: Oceans*, vol. 111, no. C1, 2006.

[37] M. Shi *et al.*, “The role of Qiongzhou Strait in the seasonal variation of the South China Sea circulation,” *Journal of Physical Oceanography*, vol. 32, no. 1, pp. 103–121, 2002.

[38] Maritime Executive. “Strait of Malacca key chokepoint for oil trade.” Accessed Feb. 20, 2020. [Online]. Available: https://www.maritime-executive.com/article/strait-of-malacca-key-chokepoint-for-oil-trade

[39] G. H. Keller and A. F. Richards, “Sediments of the Malacca Strait, Southeast Asia,” *Journal of Sedimentary Research*, vol. 37, no. 1, pp. 102–127, 1967.

[40] O. A. Godin, B. G. Katsnelson, and T. W. Tan, “Normal mode dispersion and time warping in the coastal ocean,” *Journal of the Acoustical Society of America*, vol. 146, no. 3, pp. EL205-EL211, 2019.

INITIAL DISTRIBUTION LIST

1. Defense Technical Information Center
   Ft. Belvoir, Virginia

2. Dudley Knox Library
   Naval Postgraduate School
   Monterey, California